The Astrophysical Journal, 720:64–86, 2010 September 1 doi:10.1088/0004-637X/720/1/64

IRS SCAN-MAPPING OF THE WASP-WAIST NEBULA (IRAS 16253−2429). I. DERIVATION OF SHOCK CONDITIONS FROM H_2 EMISSION AND DISCOVERY OF 11.3 μm PAH ABSORPTION

Mary Barsony[1,5], Grace A. Wolf-Chase[2,6], David R. Ciardi[3], and JoAnn O'Linger[4]
[1] Department of Physics & Astronomy, San Francisco State University, 1600 Holloway Drive, San Francisco, CA 94132, USA; mbarsony@stars.sfsu.edu
[2] Astronomy Department, Adler Planetarium, 1300 South Lake Shore Drive, Chicago, IL 60605, USA; gwolfchase@adlerplanetarium.org
[3] NASA Exoplanet Science Institute/Caltech, 770 South Wilson Avenue, MS 100-22, Pasadena, CA 91125, USA; ciardi@ipac.caltech.edu
[4] Spitzer Science Center, California Institute of Technology MS 314-6, Pasadena, CA 91125, USA; joanno@ipac.caltech.edu
Received 2010 February 24; accepted 2010 June 30; published 2010 August 5

ABSTRACT

The outflow driven by the Class 0 protostar, IRAS 16253−2429, is associated with bipolar cavities visible in scattered mid-infrared light, which we refer to as the Wasp-Waist Nebula. InfraRed Spectometer (IRS) scan mapping with the *Spitzer Space Telescope* of a $\sim 1' \times 2'$ area centered on the protostar was carried out. The outflow is imaged in six pure rotational (0-0 $S(2)$ through 0-0 $S(7)$) H_2 lines, revealing a distinct, S-shaped morphology in all maps. A source map in the 11.3 μm polycyclic aromatic hydrocarbon (PAH) feature is presented in which the protostellar envelope appears in absorption. This is the first detection of absorption in the 11.3 μm PAH feature. Spatially resolved excitation analysis of positions in the blue- and redshifted outflow lobes, with extinction-corrections determined from archival *Spitzer* 8 μm imaging, shows remarkably constant temperatures of $\sim$1000 K in the shocked gas. The radiated luminosity in the observed H_2 transitions is found to be $1.94 \pm 0.05 \times 10^{-5}$ $L_\odot$ in the redshifted lobe and $1.86 \pm 0.04 \times 10^{-5}$ $L_\odot$ in the blueshifted lobe. These values are comparable to the mechanical luminosity of the flow. By contrast, the mass of hot ($T \sim 1000$ K) H_2 gas is $7.95 \pm 0.19 \times 10^{-7}$ $M_\odot$ in the redshifted lobe and $5.78 \pm 0.17 \times 10^{-7}$ $M_\odot$ in the blueshifted lobe. This is just a tiny fraction, of order 10^{-3}, of the gas in the cold (30 K), swept-up gas mass derived from millimeter CO observations. The H_2 *ortho/para ratio* of 3:1 found at all mapped points in this flow suggests previous passages of shocks through the gas. Comparison of the H_2 data with detailed shock models of Wilgenbus et al. shows the emitting gas is passing through Jump (J-type) shocks. Pre-shock densities of 10^4 cm^{-3} $\leqslant n_H \leqslant 10^5$ cm^{-3} are inferred for the redshifted lobe and $n_H \leqslant 10^3$ cm^{-3} for the blueshifted lobe. Shock velocities are 5 km s^{-1} $\leqslant v_s \leqslant$ 10 km s^{-1} for the redshifted gas and $v_s = 10$ km s^{-1} for the blueshifted gas. Initial transverse (to the shock) magnetic field strengths for the redshifted lobe are in the range 10–32 μG, and just 3 μG for the blueshifted lobe. A cookbook for using the CUBISM contributed software for IRS spectral mapping data is presented in the Appendix.

Key words: infrared: ISM – ISM: jets and outflows – ISM: magnetic fields – stars: formation – stars: individual (IRAS 16253−2429) – stars: protostars

Online-only material: color figures

1. INTRODUCTION

The Wasp-Waist Nebula is so-named because of its appearance in archival Infrared Array Camera[7] (IRAC) images from the *Spitzer Space Telescope* (Barsony et al. 2005; see Figure 1(a)). The term "wasp-waist" refers to a silhouette, whose primary feature is the abrupt transition from a natural-width rib cage to an exceedingly small waist, with the hips curving out below. It takes its name from its similarity to a wasp's segmented body. An external constricting force is required to produce this shape: a corset in humans, a dense protostellar envelope in the equatorial plane in the case of the Wasp-Waist Nebula. The color-composite IRAC image in Figure 1(a), constructed from individual filter gray-scale images in the *Spitzer* archive, shows a beautiful, bipolar hourglass structure, tracing the outflow cavities, in addition to shock features from the flow. The protostellar envelope is seen in absorption, most prominently in the 8.0 μm image. Figure 1(b) shows a cartoon schematic separating out the different source components: the protostellar envelope in maroon, the scattered-light bipolar cavity in the background gray-scale image, and the mid-infrared (mid-IR) H_2 shock emission in yellow.

The central powering engine of this nebula is the Class 0 protostar, IRAS 16253−2429, whose bipolar molecular outflow was first detected by ground-based imaging of its 2.12 μm H_2 and CO(3→2) emissions (Khanzadyan et al. 2004; Stanke et al. 2006, respectively).

Although located in the intensively studied ρ Oph star-forming region, IRAS 16253−2429 had eluded recognition as a Class 0 protostar for over two decades because of its relatively "remote" location (at $\sim 1/2^\circ$ separation) from its famous cousin, VLA1623 (André et al. 1993). IRAS 16253−2429 resides in a relatively isolated, quiescent portion of the ρ Oph clouds, to the east of the ρ Oph A core, a territory unexplored by earlier millimeter continuum and *Infrared Space Observatory* (*ISO*) studies of the cloud (e.g., Motte et al. 1998; Bontemps et al. 2001).

The *IRAS* satellite did not detect this object at its two shortest wavelengths, 12 μm and 25 μm, and it remains undetected from the ground at 2 μm (Khanzadyan et al. 2004). Being a strong 1.1 mm continuum source in the large-area *SEST* (the now defunct Swedish-ESO Submillimeter Telescope) survey of the ρ Oph clouds, and located at the center of weak H_2 and CO(3→2) flows, Stanke et al. (2006) proposed this object, their MMS126, as a Class 0 candidate.

[5] Also at Space Science Institute, 4750 Walnut Street, Suite 205, Boulder, CO 80301, USA.
[6] Also at Department of Astronomy & Astrophysics, University of Chicago, 5640 South Ellis Avenue, Chicago, IL 60637, USA.
[7] Fazio et al. (2004).

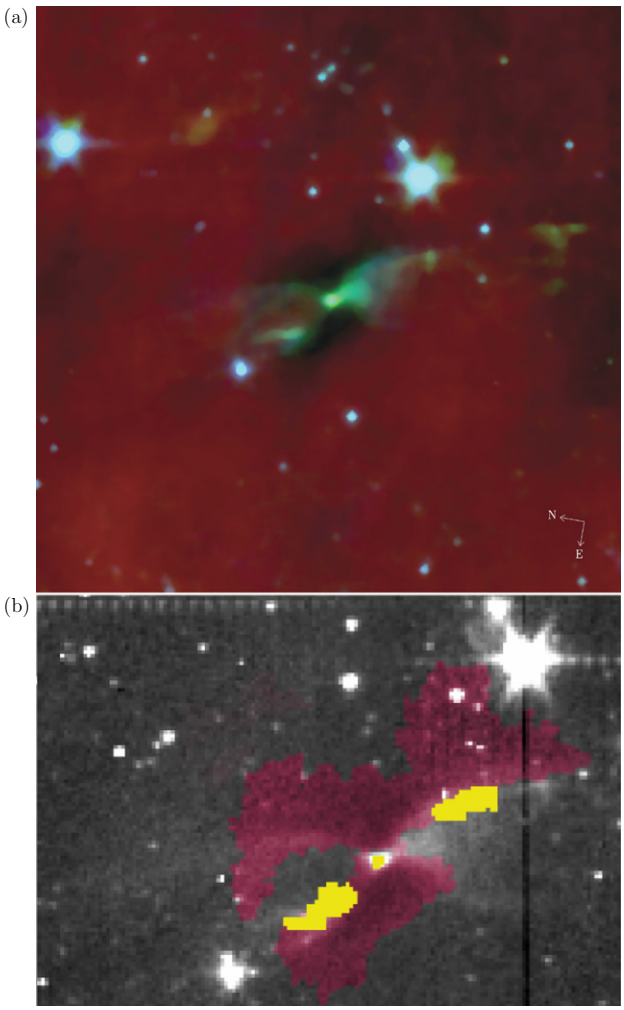

Figure 1. (a) Composite 3 color IRAC image of the Wasp-Waist Nebula, acquired from archival c2d *Spitzer* data. Blue = IRAC Channel 1 (3.6 μm), green = IRAC Channel 2 (4.5 μm), and red = IRAC Channel 4 (8.0 μm). Note the dark absorption produced by the infall envelope absorbing against the bright PAH emission from the cloud. (b) Cartoon schematic of the protostellar envelope, as traced by absorption at 8.0 μm in IRAC Channel 4 (maroon) overlaid on the 3.6 μm IRAC Channel 1 image (background grayscale) which shows the scattered light from the bipolar cavity walls of the envelope most prominently. Our IRS results show that the pure molecular hydrogen line emission (shown in yellow) is distributed in an S-shape, along the cavity walls.

The bolometric luminosity of IRAS 16253, as determined from the best two-temperature fit to the source's continuum spectral energy distribution, including IRAC, MIPS, *IRAS*, and *SEST* detections, is just 0.27 $\pm$ 0.03 $L_{\odot}$ (M. Barsony et al. 2010, in preparation). The envelope's mass, determined from its millimeter continuum emission, is 0.15 $M_{\odot}$, which agrees well with the mass derived from the $\tau_{8\,\mu m}$ map obtained with *Spitzer* (Stanke et al. 2006; M. Barsony et al. 2010, in preparation).

What makes IRAS 16253−2429 truly unique, however, is that at mid-infrared wavelengths, its infall envelope is seen in absorption against the bright, polycyclic aromatic hydrocarbon (PAH) feature and graphitic very small grain (VSG) continuum emission excited by the UV radiation of the B stars behind the ρ Oph cloud along our line-of-sight. In fact, the ρ Oph cloud stands alone among the well-studied, nearby ($d \leqslant 350$ pc) star-forming clouds such as Taurus, Lupus, Chamaeleon, R Corona Australis, Serpens, and Perseus, in that it is brightly glowing in the mid-infrared, especially the PAH features, since it is back-lit by the Sco-Cen OB association (e.g., Abergel et al. 1996).

One motivation for obtaining InfraRed Spectrometer (IRS) spectral maps of the Wasp-Waist Nebula was to distinguish the pure shocked molecular line outflow emission at mid-infrared wavelengths from the scattered light of the outflow cavities so beautifully evident in the IRAC images (see Figure 1) and from the PAH emission ubiquitously found throughout the ρ Ophiuchi cloud core. In fact, very few, if any, protostellar sources have observations separating the outflow from the outflow cavity in the region where both structures overlap (see Ybarra et al. 2006 for an example in the case of a late-stage protostar). A second goal of the IRS mapping was to study the absorption envelope of IRAS 16253−2429 in detail, to infer its density structure and morphology. This is the topic of a separate, forthcoming paper (M. Barsony et al. 2010, in preparation). However, in the process, we have discovered that the envelope of IRAS 16253−2429 is seen in absorption in the 11.3 μm PAH feature (see Sections 3.3 and 4.2).

Mid-infrared spectral scan maps of the Wasp-Waist Nebula were acquired with the InfraRed Spectrometer (IRS; Houck et al. 2004) aboard the *Spitzer Space Telescope* (Werner et al. 2004). The brightest outflow emission regions, as determined from ground-based 2.12 μm H_2 imaging, were mapped.

Spitzer's exquisite sensitivity resulted in spatially resolved maps of the outflow in six different mid-infrared H_2 transitions. Additionally, a map of the protostellar envelope and its immediate environs in the 11.3 μm PAH feature is presented, in which this feature is found *in absorption* for the first time. From the H_2 mapping data, excitation diagrams and gas temperatures are derived as a function of position in the flow. Since the H_2 emission is optically thin, the gas mass in the imaged portion of the flow is calculated, independently of orientation effects. The H_2 line data are consistent with emission from J-shocks rather than C-shocks. Comparison with J-shock models constrains the physical parameters of the pre-shock gas. For the blueshifted outflow lobe, pre-shock densities are $n_H \leqslant 10^3$ cm^{-3}, the shock velocity is 10 km s^{-1}, and the magnetic field strength, transverse to the shock propagation direction, is 3.2 μG. These quantities are $10^4 \leqslant n_H \leqslant 10^5$ cm^{-3}, 5 km s^{-1} $\leqslant v_s \leqslant$ 10 km s^{-1}, and 10 μG $\leqslant B \leqslant$ 32 μG, respectively, for the redshifted lobe. The initial *ortho-to-para ratio* (*opr*) of the gas had to be high, 3:1, in order to account for the presently observed value of *opr* = 3. This means that the ambient gas into which the currently observed gas propagates had to already have been heated previously by earlier shocks.

The observations and data reduction procedures are described in Section 2, our results are presented in Section 3, the interpretation of the results and ancillary data are found in the discussion, Section 4, and our conclusions, in summary form, are recapitulated in Section 5. The Appendix describes the use of the IDL-based CUBISM program for the reduction and analysis of IRS spectral mapping data in detail.

2. OBSERVATIONS AND DATA REDUCTION

2.1. Data Acquisition

Spectral scan maps with the IRS instrument aboard the *Spitzer Space Telescope* were acquired on 2007 March 19. A total of six Astronomical Observation Requests (AORs) were executed to perform maps of the target through the two low spectral resolution slits (3.″6 ×57″) known as SL1 (Short-Low Module 1, 7.54–14.7 μm, with $\lambda/\Delta\lambda$ = 64–128), and SL2 (Short-Low Module 2, 5.2–7.6 μm, $\lambda/\Delta\lambda$ = 80–128).

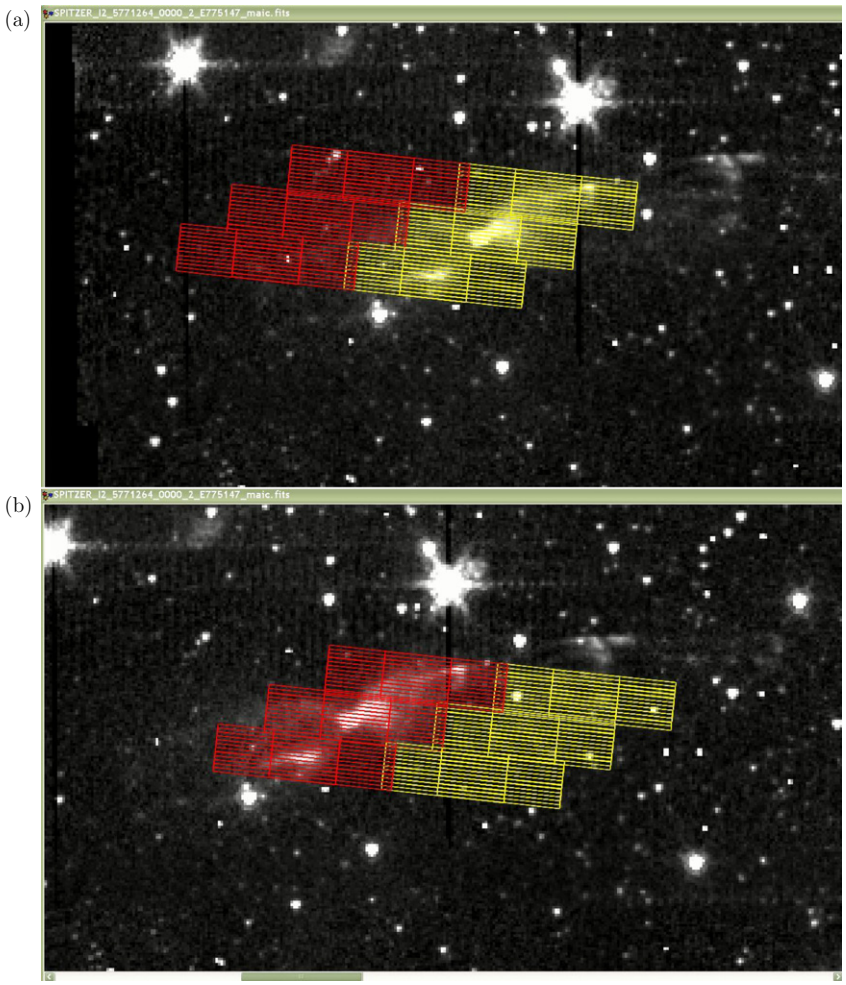

Figure 2. Schematic overlay of the IRS slits on the IRAC 4.5 μm image of the Wasp-Waist Nebula. The SL2 (5.2–7.6 μm) slit positions are outlined in yellow, while the SL1 (7.54–14.7 μm) slit positions are outlined in red. Panel (a) shows the SL2-centered map and the SL1 off-source, background map. Panel (b) shows the SL1-centered map and the SL2 off-source, background map.

Figure 2 shows the SL1 (red) and SL2 (yellow) slit positions overlaid on the IRAC 4.5 μm (Channel 2) image of the Wasp-Waist Nebula. The total spatial extent of the final on-source maps is 136.″9 × 62.″9 (corresponding to 72 × 34 projected pixels on the sky, at 1.″850 pixel^{-1}).

Figure 2(a) shows the SL2 centered spectral map (yellow outlines), consisting of three AORs: 19063808, 19063296, and 19063552, from top to bottom, respectively. Each AOR consisted of 11 (perpendicular to the slit) × 2 (along the slit) map points, with 1/2 slit overlap, in both directions, for full Nyquist sampling. Since data from both low spectral resolution slits are acquired on the same detector simultaneously, off-source data from the SL1 slit (shown in red) were acquired during the on-source SL2 (shown in yellow) observations. These SL1 off-source data are used as the background measurement for processing of the SL1 centered map, shown in Figure 2(b).

Figure 2(b) shows the SL1 centered (red outlines) spectral map, consisting of AORs, 19063040, 19062528, and 19062784, from top to bottom, respectively. Data were taken in the same manner as for the SL2 centered map. The off-source SL2 data acquired during the on-source SL1 observations were subsequently used as the background for processing of the SL2-centered maps.

Total on-source integration times at each map point were 205.53 s for the two AORs centered on the protostar and 190.85 s for the four AORs offset from the central protostellar position. To avoid chip saturation, we were forced to use short, 14.68 s (eight "samples up the ramp;" Rieke 2007), exposure times at each slit position, repeated 14 times for the maps centered on the protostar (AORs 19062528 and 19063296), and repeated 13 times for the four off-center maps (AORs 19063808, 19063040, offset above the protostellar position in Figures 2(a) and 2(b), and AORs 19063552 and 19062784, offset below the protostellar position in Figures 2(a) and 2(b)). If *any* portion of the array on which the SL1 and SL2 spectra are imaged becomes saturated, data from the entire chip are compromised. The 128 × 128 array on which the SL1 and SL2 spectra are acquired is also used to image blank sky (in our case), or peak-up sources (in the case of other programs) through two wide-band filters: one "blue" (13–18.5 μm) and one "red" (18.5–26 μm). Unfortunately for our program, the sky background toward our target at the time of observation was rather high, at the same time we were trying to acquire faint source spectra, necessitating use of the otherwise inefficient short integration times (of 14.68 s) per map point.

2.2. Data Processing

Spitzer Science Center (SSC) pipeline (ver. S16.1.0) processed data were downloaded with the aid of the Leopard archive query software. The "basic calibrated data" (BCDs) were the starting point for subsequent analysis. The pipeline processing from the raw satellite data to the BCD data products for the IRS SL1 and SL2 modules is described in the IRS Data Handbook

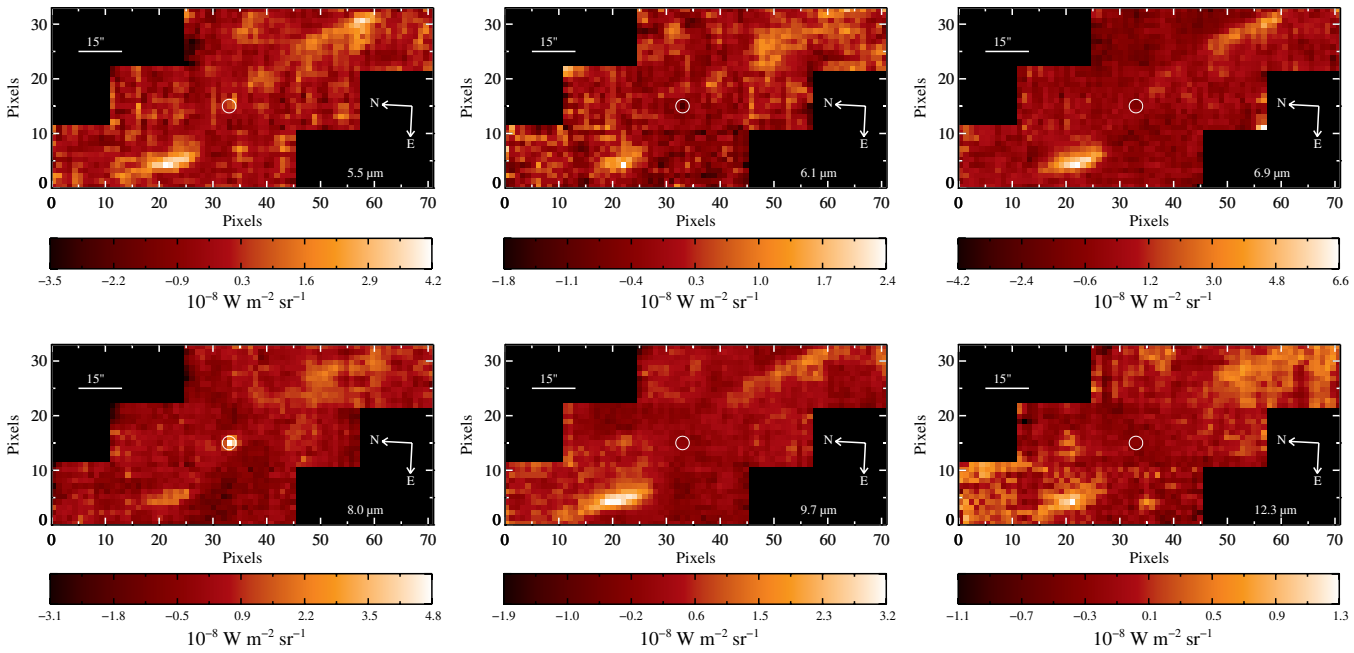

Figure 3. Integrated intensity maps of the emission from the six H_2 transitions detected in our IRS spectral scan mapping of the central 2.′25 × 1′ region of the Wasp-Waist Nebula. Line intensities in each map are color-coded according to the colorbars shown. For reference, each re-projected pixel is a square 1.″85 on a side. A scale bar of 15″ length is shown on each map, along with a compass rose showing north and east.

(A color version of this figure is available in the online journal.)

(available at http://ssc.spitzer.caltech.edu/IRS/dh/). The BCD IRS data have been dark-subtracted, flat-fielded, and flux- and wavelength-calibrated.

The software package CUBISM (the Cube Builder for IRS Spectral Mapping, Smith et al. 2007) was used for further processing and analysis of the BCD data obtained from the SSC archive. Within CUBISM, the BCD data were background-subtracted, a flux calibration using an idealized uniform source model illuminating the slit (instead of the point-source model used as the default for SSC pipeline-processed data) was applied, and "hot" pixels were corrected. Maps at 77 individual wavelengths, spanning the 5.2–7.6 μm wavelength range, were constructed from the SL2 data (72 × 34 reconstructed pixels). Maps at 117 individual wavelengths, spanning the 7.54–14.7 μm wavelength range, were constructed from the SL1 data. CUBISM also allows extraction of one-dimensional (1-D) spectra from within a user-specified polygonal aperture. Detailed discussion of data processing and analysis within CUBISM is deferred to the Appendix.

3. RESULTS

3.1. H_2 Line Maps

The IRS spectral scan maps of the Wasp-Waist Nebula in all of the pure rotational transitions in the ground vibrational state of the H_2 molecule within the SL modules' bandpass (5.2–14.7 μm) are shown in Figure 3. The mid-IR H_2 transitions detected, their wavelengths, Einstein A (spontaneous radiative decay) coefficients, and E_u/k, upper level energies divided by Boltzmann's constant, are given in Table 1. The position of the protostar is indicated by a white circle in each panel of Figure 3. In stark contrast to the bipolar morphology of the scattered light nebula, evident in Figure 1, the H_2 morphology, which traces where the outflow is shocking the ambient gas, is distinctly S-shaped, displaying point symmetry about the protostar, in all of the observed transitions.

Table 1
Mid-infrared H_2 Line Properties

λ (μm)	Transition[a]	J[b]	J'[c]	g_J[d]	E_u/k[e] (K)	A[f] (s^{-1})
12.2785	0-0 $S(2)$	4	2	9	1682	2.75×10^{-9}
9.66491	0-0 $S(3)$	5	3	33	2505	9.83×10^{-9}
8.02505	0-0 $S(4)$	6	4	13	3476	2.64×10^{-8}
6.90952	0-0 $S(5)$	7	5	45	4588	5.88×10^{-8}
6.10856	0-0 $S(6)$	8	6	17	5832	1.14×10^{-7}
5.51116	0-0 $S(7)$	9	7	57	7200	2.00×10^{-7}

Notes.
[a] Transitions are designated by 0-0 $S(J')$, where 0-0 denotes the change in vibrational level, and the number in parenthesis is the FINAL rotational level. S indicates $\Delta J = -2$.
[b] Initial (upper) rotational state.
[c] Final (lower) rotational state.
[d] The statistical weight, g_J, is the product of the nuclear spin statistical weight, g_S, and the rotational statistical weight, $2J + 1$. $g_S = 1$ for the *para* states and $g_S = 3$ for the *ortho* states. The rotational numbers are odd for the *ortho* lines and even for the *para* lines.
[e] Dabrowski (1984) gives the upper level energies in units $\lambda^{-1} = E_u/hc$. Multiply by hc/k to get listed values.
[f] Transition probabilities are taken from Wolniewicz et al. (1998).

3.2. Spectral Variation along Flow Lobes

In order to study the variation of excitation conditions along the flow, we examined spectra through the apertures shown in Figure 4.[8] Central coordinates for each aperture are listed in Table 2. Each aperture has dimensions of 7.″40 × 7.″40 (4 pixels × 4 pixels). The protostar is located in Aperture 1.

Combined SL2 (5.2–7.6 μm) + SL1 (7.54–14.7 μm) spectra for each aperture are displayed in Figures 5(a) and 5(b), starting

[8] Aperture 6 is missing for historical reasons. It was inadvertently assigned zero area in a DS9 regions file early on in the analysis. Subsequent renumbering of all of the apertures would have no significance.

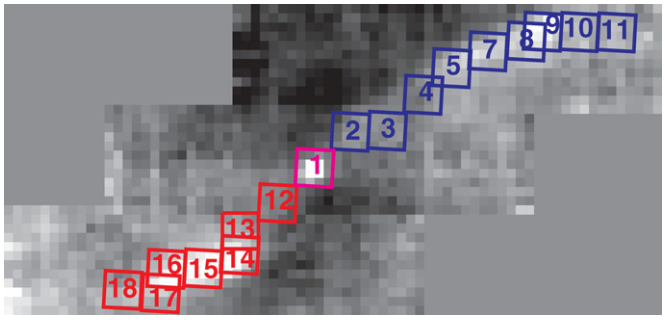

Figure 4. Apertures, each 7.″40 (4 pixels) on a side, used for studying spectral variations as a function of position in the outflow driven by the central protostar of the Wasp-Waist Nebula (indicated by the magenta box as Aperture 1). Apertures colored blue are in the blueshifted outflow lobe (as determined from CO (3–2) observations; Stanke et al. 2006). Apertures colored red are in the redshifted outflow lobe. The background grayscale image shows the integrated line intensity map of the emission from all of the H_2 transitions detected in our IRS/SL mapping. Coordinates of aperture centers are listed in Table 2.

(A color version of this figure is available in the online journal.)

from the protostellar position, moving outward (upward in each figure) along the blue and redshifted lobes, respectively. Each spectrum is labeled by its aperture number, as listed in Table 2. The positions of the emission lines at each of the six H_2 wavelengths mapped in Figure 3 and tabulated in Table 1 are labeled and indicated by vertical lines above the spectra displayed in Figures 5(a) and 5(b). The horizontal dashed lines plotted with each spectrum indicate the zero level. With the exception of the protostellar (Aperture 1) spectrum, each subsequent spectrum is offset by a constant value for clarity. Vertical axis units are MJy sr^{-1}, so the calibrated spectra, referenced to each individual spectrum's zero level, can easily be inter-compared. The SL1 and SL2 spectra overlap in the 7.5−7.6 μm region. Apart from editing out either the last few (noisy) SL2 or first few (noisy) SL1 datapoints from a given spectrum, no other editing or off-setting between the two spectral modules was necessary when joining these spectra. This attests to the excellent background subtraction and flux calibration of the data, since the backgrounds for each module were obtained from different on-sky positions (see Figure 2) and were processed independently.

In addition to the rotational transitions of the H_2 molecule detected in the ground vibrational state, we also searched for emission from the H_2 1-1 $S(5)$ line at 7.2807 μm and the H_2 1-1 $S(7)$ line at 5.8111 μm, neither of which were detected. Similarly, none of the hydrogen recombination lines within our bandpass were detected. These are the Pfund α, H (6→5) line at 7.4598828 μm, the Humphreys β, H (8→6) line at 7.5025107 μm, and the Humphreys α, H (7→6) line at 12.3719287 μm. This latter is rather close in wavelength to the 12.2785 μm H_2 0-0 $S(2)$ line, but would have been resolved from it in our spectra, had it been detected. Characteristic ionic lines associated with predominantly ionized media (e.g., Rosenthal et al. 2000), such as [Ar III] at 8.9 μm, [S IV] at 10.5 μm, and [Ne II] at 12.8 μm, are not detected. Although the [Ar II] line at 6.985 μm would be separated from the H_2 0-0 $S(5)$ line at 6.909 μm by only two spectral channels at our resolution, and thus, be only marginally resolved, at best, our results—giving tight constraints on the derived H_2 temperatures—see Section 4.3.2, make it unlikely that [Ar II] is detected at any significant level in our spectra. Of the previously reported ionic lines that are detected in protostellar outflows that fall within the bandpass of the SL1+SL2 modules (e.g., Neufeld et al. 2006; Rosenthal et al. 2000), neither the [Fe II] line at 5.3403 μm, nor the [Ni II] line at 6.636 μm are detected. These non-detections are consistent with the low-velocity, non-dissociative shocks giving rise to the observed H_2 emission (see Section 4.3.3).

Table 2
Aperture IDs, Coordinates, and Opacities in the Wasp-Waist Nebula Flow

Aperture ID[a]	R.A. J2000			Decl. J2000)			$\tau_{8\,\mu m}$[b]	A_K (mag)
	h	m	s	°	′	″		
1	16	28	21.605	−24	36	24.99	0.153 ± 0.085	0.37
2	16	28	21.040	−24	36	31.85	0.136 ± 0.044	0.33
3	16	28	20.996	−24	36	39.23	0.106 ± 0.028	0.26
4	16	28	20.433	−24	36	46.17	0.072 ± 0.032	0.17
5	16	28	20.015	−24	36	51.57	0.038 ± 0.039	0.092
7	16	28	19.846	−24	36	58.82	0.014 ± 0.024	0.033
8	16	28	19.560	−24	37	06.13	0.009 ± 0.014	0.022
9	16	28	19.400	−24	37	09.60	0.007 ± 0.018	0.016
10	16	28	19.376	−24	37	17.03	−0.004 ± 0.013[c]	0.00
11	16	28	19.351	−24	37	24.53	0.005 ± 0.014	0.01
12	16	28	22.158	−24	36	17.91	0.122 ± 0.050	0.295
13	16	28	22.599	−24	36	10.72	0.073 ± 0.045	0.177
14	16	28	22.956	−24	36	10.84	0.116 ± 0.074	0.280
15	16	28	23.185	−24	36	03.64	0.040 ± 0.059	0.096
16	16	28	23.221	−24	35	56.15	0.032 ± 0.021	0.078
17	16	28	23.632	−24	35	55.01	0.035 ± 0.029	0.084
18	16	28	23.656	−24	35	47.66	0.043 ± 0.010	0.104

Notes.
[a] Apertures are plotted in Figure 4.
[b] Median values derived in boxes 10 IRAC pixels on a side, centered on the coordinates for the given aperture.
[c] The statistics are such that mean is easily skewed by outliers (both positive and negative).

Line strengths through each aperture were measured using CUBISM as detailed in the Appendix, part 6. (b) "Line Flux Measurement." The results for each aperture are listed in Table 3.

For collisionally excited H_2 gas in local thermodynamic (statistical) equilibrium at a single kinetic temperature, T, the column density distribution is given by

$$\frac{N(v, J)}{g_J} = N_{H_{2,\rm tot}} \frac{e^{-E(v,J)/kT}}{\Sigma_{v',J'} g_{J'} e^{-E(v',J')/kT}}. \quad (1)$$

For this reason, it is common to plot "excitation diagrams," which are plots of the natural logarithm of the upper level column densities, N_u, divided by the level degeneracy, g_J, versus E_u/k, the upper level energies divided by the Boltzmann constant, k. The slope of the resultant line is $-1/T$, the negative inverse of the kinetic temperature, T.

The column densities are derived from the measured line intensities, $I_{\rm obs}(v, J \rightarrow v', J')$ listed in Table 3 for each aperture, from the equation:

$$N_{\rm obs}(v, J) = \frac{4\pi\lambda}{hc} \frac{I_{\rm obs}(v, J \rightarrow v', J')}{A(v, J \rightarrow v', J')}. \quad (2)$$

Each observed transition's wavelength, λ, is listed in Column 1 of Table 1. Corresponding Einstein coefficients, $A(v, J \rightarrow v', J')$, are listed in Column 7 of Table 1 (Wolniewicz et al. 1998). The level degeneracy of a rotational transition for the H_2 molecule is given by

$$g_J = g_S(2J + 1), \quad (3)$$

Table 3
Line Strengths, Extinctions, and Column Densities

Aperture ID	λ (μm)	Integrated Line Strength[a] (MJy sr^{-1} μm)	I_{obs}[b] (10^{-6} erg s^{-1} cm^{-2} sr^{-1})	N_u(obs) (10^{16} cm^{-2})	A_λ	N_u[c] (10^{16} cm^{-2})	$\ln(N_u/g_J)$
1	12.2785	<0.0830[d]	<1.65	<4.66	0.175	<5.48	36.34481386
	9.66491	<0.03[d]	<0.963	<0.599	0.497	<0.946	33.28968279
	8.02505	0.354 ± 0.05	16.5	3.17	0.166	3.69 ± 0.608	35.58208352
	6.90952	0.0691 ± 0.04	4.34	0.323	0.166	0.376 ± 0.220	32.05581646
	6.10856	<0.023[d]	<1.83	<0.0619	0.166	<0.072	<30.28029103
	5.51116	0.021568 ± 0.01	2.13	0.0371	0.166	0.0432 ± 0.204	29.65696086
2	12.2785	<0.0294[d]	<0.585	<1.65	0.156	<1.90	<35.2893259
	9.66491	<0.290[d]	<9.30	<5.78	0.442	<8.69	<35.5070385
	8.02505	0.156 ± 0.03	7.28	1.40	0.147	1.60 ± 0.32	34.74815237
	6.90952	0.113 ± 0.01	7.11	0.528	0.147	0.605 ± 0.060	32.53231504
	6.10856	<0.049[d]	<3.94	<0.134	0.147	<0.153	<32.1311715
	5.51116	<0.0959[d]	<9.46	<0.165	0.147	<0.189	<31.13173785
3	12.2785	0.0840 ± 0.02	1.67	4.72	0.122	5.28 ± 1.26	36.30726374
	9.66491	0.0775 ± 0.02	2.49	1.55	0.346	2.13 ± 0.560	34.10010201
	8.02505	0.0436 ± 0.01	2.03	0.390	0.115	0.434 ± 0.100	33.44197258
	6.90952	0.0862 ± 0.01	5.41	0.402	0.115	0.448 ± 0.053	32.23076528
	6.10856	<0.005[d]	<0.403	<0.0136	0.115	<0.0152	<29.82023671
	5.51116	<0.031[d]	<3.05	<0.0531	0.115	<0.0590	<29.96844017
4	12.2785	0.089 ± 0.015	1.77	5.0	0.082	5.39 ± 0.914	36.32927516
	9.66491	0.170 ± 0.022	5.46	3.4	0.234	4.21 ± 0.583	34.78292567
	8.02505	0.141 ± 0.027	6.55	1.26	0.078	1.35 ± 0.263	34.57852085
	6.90952	0.020 ± 0.005[e]	1.27	0.0942	0.078	0.101 ± 0.0253	30.74456097
	6.10856	<0.041[d]	<3.27	<0.111	0.078	<0.119	<31.88052305
	5.51116	<0.010[d]	<0.997	<0.0174	0.078	<0.0187	<28.81761825
5	12.2785	0.161 ± 0.026	3.20	9.03	0.044	9.40 ± 1.53	36.88463095
	9.66491	0.231 ± 0.019	7.43	4.62	0.124	5.18 ± 0.508	34.98938262
	8.02505	0.166 ± 0.019	7.74	1.49	0.041	1.55 ± 0.187	34.7115639
	6.90952	0.284 ± 0.018	17.9	1.33	0.041	1.38 ± 0.102	33.35593516
	6.10856	0.097 ± 0.0096	7.78	0.264	0.041	0.274 ± 0.0292	32.71279197
	5.51116	0.096 ± 0.0097	9.51	0.166	0.041	0.172 ± 0.0186	31.03948499
7	12.2785	0.187 ± 0.01	3.71	10.5	0.016	10.6 ± 0.583	37.00808245
	9.66491	0.292 ± 0.02	9.38	5.84	0.045	6.08 ± 0.461	35.15053342
	8.02505	0.197 ± 0.02	9.16	1.76	0.015	1.79 ± 0.187	34.85676306
	6.90952	0.361 ± 0.02	22.7	1.69	0.015	1.71 ± 0.103	33.57234058
	6.10856	0.071 ± 0.01	5.70	0.193	0.015	0.196 ± 0.028	32.37775063
	5.51116	0.162 ± 0.02	16.0	0.279	0.015	0.283 ± 0.036	31.53681305
8	12.2785	0.158 ± 0.02	3.14	8.87	0.010	8.96 ± 1.14	36.83647685
	9.66491	0.362 ± 0.02	11.6	7.22	0.029	7.42 ± 0.432	35.34920166
	8.02505	0.314 ± 0.03	14.6	2.81	0.0097	2.84 ± 0.274	35.31918267
	6.90952	0.360 ± 0.02	22.6	1.68	0.0097	1.69 ± 0.0969	33.56125092
	6.10856	0.039 ± 0.01	3.17	0.107	0.0097	0.108 ± 0.0275	31.78537076
	5.51116	0.228 ± 0.02	22.5	0.393	0.0097	0.396 ± 0.0351	31.87300072
9	12.2785	0.211 ± 0.02	4.20	11.8	0.008	11.9 ± 1.14	37.12379128
	9.66491	0.347 ± 0.02	11.1	6.93	0.022	7.07 ± 0.442	35.30081154
	8.02505	0.314 ± 0.03	14.6	2.81	0.0073	2.83 ± 0.275	35.31676112
	6.90952	0.343 ± 0.02	21.5	1.60	0.0073	1.61 ± 0.0983	33.51127293
	6.10856	0.092 ± 0.02	7.41	0.251	0.0073	0.253 ± 0.055	32.63319619
	5.51116	0.207 ± 0.02	20.4	0.356	0.0073	0.359 ± 0.0352	31.77284197
10	12.2785	0.197 ± 0.03	3.92	11.1	0.00	11.1 ± 1.68	37.04881574
	9.66491	0.191 ± 0.04	6.12	3.81	0.00	3.81 ± 0.793	34.68215143
	8.02505	0.023 ± 0.004	1.07	0.205	0.00	0.205 ± 0.0359	32.69324403
	6.90952	0.154 ± 0.02	9.64	0.717	0.00	0.717 ± 0.0935	32.70195617
	6.10856	0.074 ± 0.02	5.91	0.200	0.00	0.200 ± 0.0543	32.399883
	5.51116	0.078 ± 0.02	7.73	0.135	0.00	0.135 ± 0.0343	30.79370118
11	12.2785	0.131 ± 0.02	2.60	7.33	0.005	7.36 ± 1.13	36.64086871
	9.66491	0.085 ± 0.02	2.72	1.69	0.015	1.72 ± 0.406	33.88495865
	8.02505	0.027 ± 0.01	1.25	0.241	0.0048	0.242 ± 0.090	32.85678279
	6.90952	0.211 ± 0.03	13.3	0.986	0.0048	0.990 ± 0.141	33.02507829
	6.10856	0.060 ± 0.01	4.81	0.163	0.0048	0.164 ± 0.0274	32.1995591
	5.51116	<0.03	<2.96	<0.0516	0.0048	<0.0518	<29.83888883
12	12.2785	0.069 ± 0.01	1.36	3.85	0.141	4.38 ± 0.654	36.1211804
	9.66491	0.113 ± 0.04	3.63	2.26	0.399	3.26 ± 1.19	34.5277506
	8.02505	0.104 ± 0.03	4.85	0.933	0.133	1.05 ± 0.310	34.3294647
	6.90952	<0.047[d]	<2.93	<0.219	0.133	<0.246	<31.63300321

Table 3
(Continued)

Aperture ID	λ (μm)	Integrated Line Strength[a] (MJy sr^{-1} μm)	I_{obs}[b] (10^{-6} erg s^{-1} cm^{-2} sr^{-1})	$N_u(obs)$ (10^{16} cm^{-2})	A_λ	N_u[c] (10^{16} cm^{-2})	ln(N_u/g_J)
	6.10856	<0.060[d]	<4.82	<0.163	0.133	<0.185	<32.31908359
	5.51116	<0.079[d]	<7.81	<0.136	0.133	<0.0154	<30.92653742
13	12.2785	0.116 ± 0.02	2.31	6.53	0.084	7.06 ± 1.22	36.59808792
	9.66491	0.306 ± 0.02	9.82	6.11	0.239	7.61 ± 0.706	35.37460747
	8.02505	0.118 ± 0.03	5.48	1.05	0.080	1.13 ± 0.293	34.40176416
	6.90952	0.191 ± 0.02	12.0	0.891	0.080	0.959 ± 0.109	32.99259698
	6.10856	<0.060[d]	<4.82	<0.163	0.080	<0.176	<32.27000303
	5.51116	0.028 ± 0.003	2.80	0.0488	0.080	0.0525 ± 0.006	29.85187931
14	12.2785	0.191 ± 0.02	3.81	10.8	0.133	12.2 ± 1.35	37.14299203
	9.66491	0.555 ± 0.02	17.8	11.1	0.378	15.7 ± 1.77	36.09818254
	8.02505	0.183 ± 0.02	8.50	1.64	0.126	1.84 ± 0.242	34.88412009
	6.90952	0.476 ± 0.02	29.9	2.22	0.126	2.49 ± 0.212	33.94829788
	6.10856	0.043 ± 0.01	3.47	0.118	0.126	0.132 ± 0.0321	31.98294601
	5.51116	0.177 ± 0.01	17.5	0. 305	0.126	0.343 ± 0.0318	31.72769615
15	12.2785	0.456 ± 0.02	9.07	25.6	0.045	26.7 ± 1.40	37.92896912
	9.66491	0.770 ± 0.02	24.7	15.4	0.129	17.3 ± 1.47	36.19548795
	8.02505	0.330 ± 0.02	15.4	2.96	0.043	3.08 ± 0.260	35.40035626
	6.90952	0.655 ± 0.02	41.1	3.06	0.043	3.18 ± 0.211	34.19116138
	6.10856	0.149 ± 0.02	11.9	0.405	0.043	0.421 ± 0.0619	33.14264785
	5.51116	0.229 ± 0.02	22.6	0.394	0.043	0.410 ± 0.043	31.90558083
16	12.2785	0.297 ± 0.02	5.91	16.7	0.037	17.8 ± 1.18	37.49387035
	9.66491	0.501 ± 0.01	16.1	9.99	0.105	1.10 ± 0.395	35.74394054
	8.02505	0.077 ± 0.01	3.57	0.686	0.035	0.709 ± 0.0936	33.93230746
	6.90952	0.347 ± 0.02	21.8	1.62	0.035	1.67 ± 0.102	33.54995296
	6.10856	0.056 ± 0.01	4.52	0.153	0.035	0.158 ± 0.0283	32.165135
	5.51116	0.151 ± 0.02	14.9	0.259	0.035	0.268 ± 0.0360	31.47997441
17	12.2785	0.280 ± 0.02	5.56	15.7	0.040	16.3 ± 1.76	37.4349811
	9.66491	0.318 ± 0.03	10.2	6.35	0.114	7.05 ± 0.529	35.29834315
	8.02505	0.072 ± 0.02	3.37	0.649	0.038	0.672 ± 0.186	33.87853363
	6.90952	0.181 ± 0.02	11.4	0.844	0.038	0.875 ± 0.100	32.90063396
	6.10856	<0.069[d]	<5.51	<0.189	0.038	<0.193	<32.36460969
	5.51116	0.0985 ± 0.02	9.72	0.170	0.038	0.176 ± 0.0360	31.05855611
18	12.2785	0.105 ± 0.01	2.08	5.89	0.049	6.16 ± 0.589	36.46238937
	9.66491	0.324 ± 0.02	10.4	6.47	0.140	7.37 ± 0.477	35.34163287
	8.02505	0.189 ± 0.04	8.80	1.69	0.047	1.77 ± 0.374	34.84517746
	6.90952	0.167 ± 0.03	10.5	0.780	0.047	0.814 ± 0.146	32.82894633
	6.10856	<0.067[d]	<5.39	<0.183	0.047	<0.191	<32.35160304
	5.51116	0.154 ± 0.03	15.2	0.264	0.047	0.276 ± 0.0540	31.50997434

Notes.
[a] CUBISM output for continuum-subtracted, wavelength-integrated line strength—see the Appendix, 6. (b).
[b] Column 3 value multiplied by c/λ^2 in μm^{-1} units ($=d\nu/d\lambda$), then converted to cgs.
[c] Extinction-corrected.
[d] Upper limits are 3σ.
[e] Marginal detection.

where $g_S = 3$ for *ortho*-H_2 (odd J) and $g_S = 1$ for *para*-H_2 (even J). Values of g_J for each transition are listed in Column 5 of Table 1. Upper level energies in units of Kelvin are listed in Column 6 of Table 1 (Dabrowski 1984). For each aperture, the derived upper level column densities for each transition are listed in Column 5 of Table 3.

For producing excitation diagrams, however, extinction-corrected line fluxes and, therefore, extinction-corrected column densities, are required. We have used the IRAC 8 μm image of the nebula (available from the *Spitzer* archive) to estimate the opacity. The 8 μm emission (color-coded as red in the image presented in Figure 1(a)) is relatively uniform across the field of view. The envelope is clearly visible as a darker region around the central object, attenuating the background cloud emission.

The observed surface brightness in each pixel is the result of background cloud emission, attenuation by the line-of-sight dust, and foreground emission of the form:

$$S_\lambda = S(fg)_\lambda + S(bg)_\lambda \cdot e^{-\tau_\lambda} \quad (4)$$

where $S(fg)_\lambda$ is the foreground emission, $S(bg)_\lambda$ is the background emission, and τ_λ is the line-of-sight opacity. With an estimate of the background and foreground emissions, the line-of-sight opacity per pixel can be derived:

$$\tau_\lambda = -\ln\left[\frac{S_\lambda - S(fg)_\lambda}{S(bg)_\lambda}\right]. \quad (5)$$

Because we are interested in the large area diffuse surface brightness, we must correct the observed surface brightness to account for the complex scattering of the incident photons in the focal plane array. Essentially, we must apply an "infinite-aperture" correction. At 8 μm, the observed surface brightness is scaled by 0.74 (IRAC Data Handbook 2006).

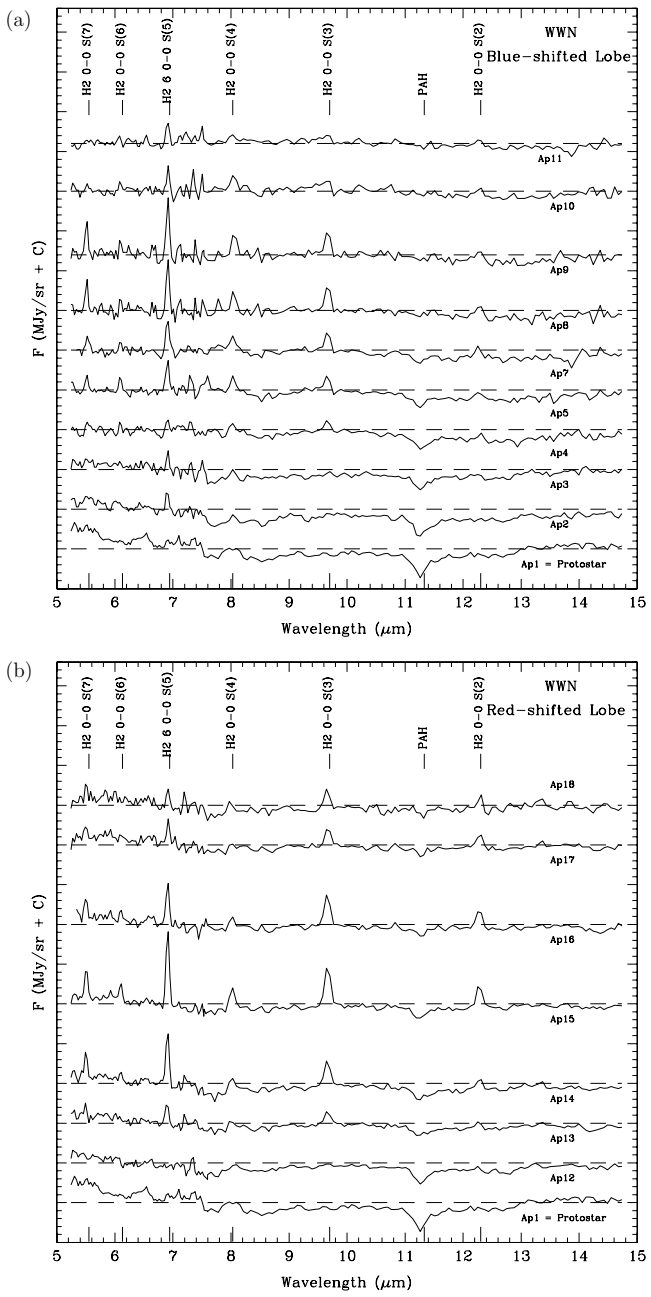

Figure 5. (a) Combined spectra (SL2 = 5.2–7.6 μm and SL1 = 7.54 –14.7 μm) as a function of position in the blueshifted outflow lobe of the Wasp-Waist Nebula: starting at the bottom with the spectrum at the protostellar position, progressing outward along the outflow lobe as one goes upwards amongst the spectra. Each spectrum is labeled by its aperture, as pictured in Figure 4 and listed in Table 2. The positions of the observed H_2 emission lines and the PAH absorption feature are labeled and indicated. The vertical scale units are spaced by 1 MJy sr^{-1}. The dashed horizontal lines through each spectrum indicate the zero level. All spectra (apart from Aperture 1 centered on the protostellar position) have been offset vertically for clarity. (b) Same as for panel (a), except for the redshifted outflow lobe: starting at the bottom with the spectrum at the protostellar position, progressing outward along the outflow lobe as one goes upward among the spectra.

At an ecliptic latitude of $\beta \approx -2.^{\circ}8$, the foreground emission along the line of sight to the nebula is dominated by the zodiacal emission of the solar system. We have used the zodiacal emission model provided by the Spitzer Science Center IRAC reduction products (IRAC Data Handbook 2006) and assumed that the zodiacal emission is responsible for the observed foreground emission ($S(fg)_\lambda = 8.206$ MJy sr^{-1}).

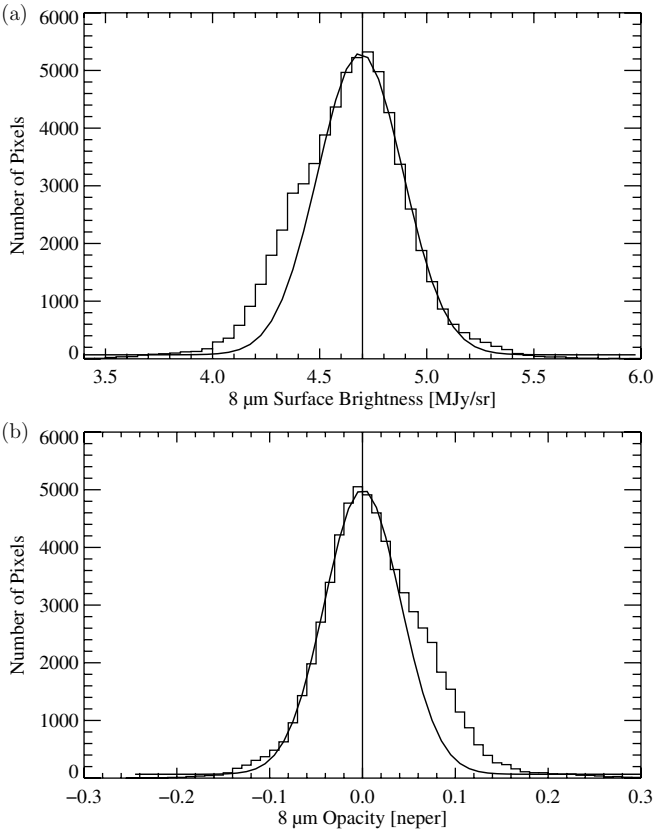

Figure 6. (a) Distribution of the 8 μm surface brightness after subtraction of the zodiacal emission. The Gaussian curve was fitted to the distribution for $4.5 \leqslant S_\nu \leqslant 6.0$ MJy sr^{-1} and has a mean $\mu = 4.7$ MJy sr^{-1} and a width $\sigma = 0.2$ MJy sr^{-1}. (b) The corresponding derived opacity distribution is shown. The opacity distribution is fitted with a Gaussian which has a mean $\mu = 0.0$ and a width $\sigma = 0.04$.

Estimating the background emission is more difficult because we have no a priori knowledge of its value. We make a primary assumption that the background emission is relatively uniform across the field and can be represented by a single value. To assess the background emission, we have fitted a Gaussian to the 8 μm surface brightness distribution (Figure 6(a)). The Gaussian fit was restricted to the surface brightness range of $4.5 \leqslant S_\nu \leqslant 6.0$ MJy sr^{-1} (after the aperture correction and foreground emission removal) to prevent bright stars and the cloud envelope opacity from skewing the fit to the distribution. The mean and width of the fitted Gaussian are $\mu = 4.7$ MJy sr^{-1} and $\sigma = 0.2$ MJy sr^{-1}. The median per pixel surface brightness uncertainty in the processed 8 μm mosaic (after scaling for the "infinite-aperture") is 0.19 MJy sr^{-1}, which demonstrates that our primary assumption of a single-value representation of the background is valid, and the measured dispersion of the diffuse emission distribution is dominated by the 8 μm flux uncertainties (as opposed to real structure in the background).

Using the 8 μm Gaussian mean as the single-value background estimate ($S(bg)_\lambda = 4.7$ MJy sr^{-1}), the opacity was calculated on a pixel-to-pixel basis from the 8 μm IRAC image. The corresponding distribution of 8 μm opacity is shown in Figure 6(b), and (as expected) has a distribution which mirrors that of the 8 μm surface brightness. The opacity distribution has also been fitted with a Gaussian that has a mean of $\mu = 0.0$ and width of $\sigma = 0.04$.

It is possible that the foreground emission from the cloud itself may be present in the observed surface brightness and that

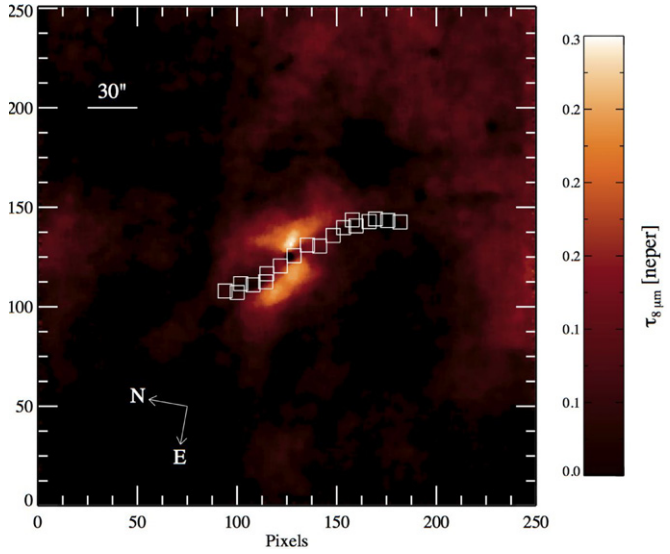

Figure 7. Map of the 8 μm optical depth toward the Wasp-Waist Nebula. The white squares represent the apertures along the flow used for subsequent spatially resolved excitation analysis. Extinction values at the wavelengths of the six observed H_2 emission lines were derived using the $\tau_{8\,\mu m}$ values derived from this map, as described in the text.

(A color version of this figure is available in the online journal.)

the zodiacal emission estimate does not sufficiently represent the foreground. Without independent observations to assess the extinction, it is difficult to disentangle the 8 μm background emission from any possible foreground emission. However, we did estimate that if 10% of the median 8 μm surface brightness (after removal of the zodiacal emission) was the result of emission in front of the envelope, then the opacity estimates would be too low by a similar fraction.

A map of $\tau_{8\mu m}$ is displayed in Figure 7. Apertures through which line fluxes were measured and for which $\tau_{8\mu m}$ were determined are outlined as white squares in this figure. For each aperture, the mean, median, and dispersion of the 8 μm opacity were determined over $12'' \times 12''$ squares (corresponding to squares of 10 IRAC pixels on a side). The resulting 8 μm opacities and their associated errors are listed in the penultimate column of Table 2.

For a given $\tau_{8\,\mu m}$, the extinction at 8 μm is $A_{8\,\mu m} = 1.0857\tau_{8\,\mu m}$. The infrared extinction law for the IRAC bands for the ρ Oph cloud, in which the Wasp-Waist Nebula resides, is given in Table 3 of Flaherty et al. (2007). Since the 5.5116 μm and 6.10856 μm lines both fall well within the IRAC 5.8 μm bandpass, we use the relation $A_{[8.0]}/A_{[5.8]} = 1.0$ for ρ Oph from Flaherty et al. (2007) to derive the extinction values for both of these lines from the $A_{8\,\mu m}$ values for each aperture. The 6.90952 μm and 8.02505 μm lines both fall within the IRAC 8.0 μm bandpass, so we simply use the $A_{8\,\mu m}$ values for each aperture for the extinction at each of these wavelengths.

The 9.66491 μm line falls right within the 9.7 μm silicate feature. Bertoldi et al. (1999) derived an empirical relation for the extinction due to the 9.7 μm silicate feature in the Orion Molecular Cloud. The shape of the feature was estimated from Draine & Lee (1984). The feature's strength (e.g., peak value) was determined relative to the extinction at 2 μm, A_K, to be $A_{9.7}/A_K = 1.35 \pm 0.15$. The A_K values for each aperture are listed in the last column of Table 2 and are derived using the relation, $A_{[8.0]}/A_{[K_S]} = 0.45 \pm 0.01$ for ρ Oph from Flaherty et al. (2007). We therefore use $A_{9.7} = 1.35 \times A_K$ for the extinction to the 9.66491 μm H_2 line.

Finally, for the extinction at the 12.2786 μm H_2 line, we apply the relation for the mid-IR extinction curve for Orion in this wavelength range, as derived by Rosenthal et al. (2000). Their Equation (2) for the mid-IR extinction curve consists of four terms: (1) the first term describes the familiar $A_\lambda \propto \lambda^{-1.7}$ law from 2 μm to 6 μm, normalized to the extinction at 2.12 μm; (2) the second term corrects for the absorption feature due to water ice at 3.05 μm; (3) the third term takes into account the effects of the 9.7 μm silicate feature; (4) the last term takes into account the effects of the 18 μm silicate feature. For estimating the extinction at 12.3 μm for our source, we ignore all but the effects of the 9.7 μm silicate feature. This leads to the following modified form of the mid-infrared extinction law derived by Rosenthal et al. (2000):

$$A_\lambda = A_{9.66\,\mu m} \times e^{-[C1\,\log(\lambda/9.66)]^2} \quad (6)$$

with $C1 = 9.8$ for $\lambda > 9.7$ μm.

Extinction-corrected column densities are derived from the observed column densities using the formula:

$$N(v, J) = N_{\rm obs}(v, J)\, 10^{0.4\,A(\lambda)} \quad (7)$$

For each aperture, Table 3 lists the detected mid-IR H_2 lines' wavelengths in Column 2; the integrated line strength within the aperture as measured with CUBISM in Column 3; the corresponding line intensity, $I_{\rm obs}(v, J \rightarrow v', J')$, in cgs units in Column 4; the observed upper level column density, N_u(obs), derived from Equation (2) in Column 5; the extinction values to each line in Column 6; the extinction-corrected upper level column density, in Column 7, and the quantity $ln(N_u/g_J)$ in Column 8.

Excitation diagrams for each aperture shown in Figure 4 were produced. Figure 8(a) shows excitation diagrams for apertures within the redshifted outflow lobe. Also included in Figure 8(a) is the excitation diagram deduced from data at the protostellar position (Aperture 1). Figure 8(b) shows the excitation diagrams for each aperture in the blueshifted outflow lobe. The straight lines plotted in each excitation diagram correspond to the best-fit excitation temperatures derived from the plotted data points, including upper limits. These are the kinetic temperatures in the local thermodynamic equilibrium (LTE) approximation.

3.3. PAH Feature Absorption in the Protostellar Envelope

There are two sources of (non-equilibrium) mid-infrared dust *emission* in the ρ Oph clouds: graphitic VSGs, ranging in size from 0.4 nm $\leqslant a \leqslant$ 10 nm, with a size distribution $n(a) \propto a^{-4}$ which account for the mid-infrared continuum emission (Draine & Anderson 1985), and the PAHs, which contain 25–40 carbon atoms, or PAH clusters, containing 50–100 carbon atoms (Siebenmorgen & Krügel 1992), which emit into several, well-known, solid state features. The PAH features that fall within the 5.2–14.7 μm spectral range of our observations include the 6.2 μm and 7.7 μm C=C stretch modes, the 8.6 μm C−H in-plane bend mode, the 11.3 μm C−H out-of-plane bend, and the 12.5 μm C−H bond resonance (e.g., Tokunaga et al. 1991; Siebenmorgen & Krügel 1992; Brooke et al. 1993; Hanner et al. 1995).

Interestingly, we detect the 11.3 μm PAH feature strongly in *absorption*, with weaker absorptions possibly detected at 7.7 μm and 8.6 μm in some of our spectra (see Figures 5(a) and 5(b)). To our knowledge, this is the first definitive detection of the 11.3 μm PAH feature in absorption in a low-mass protostellar envelope (or anywhere).

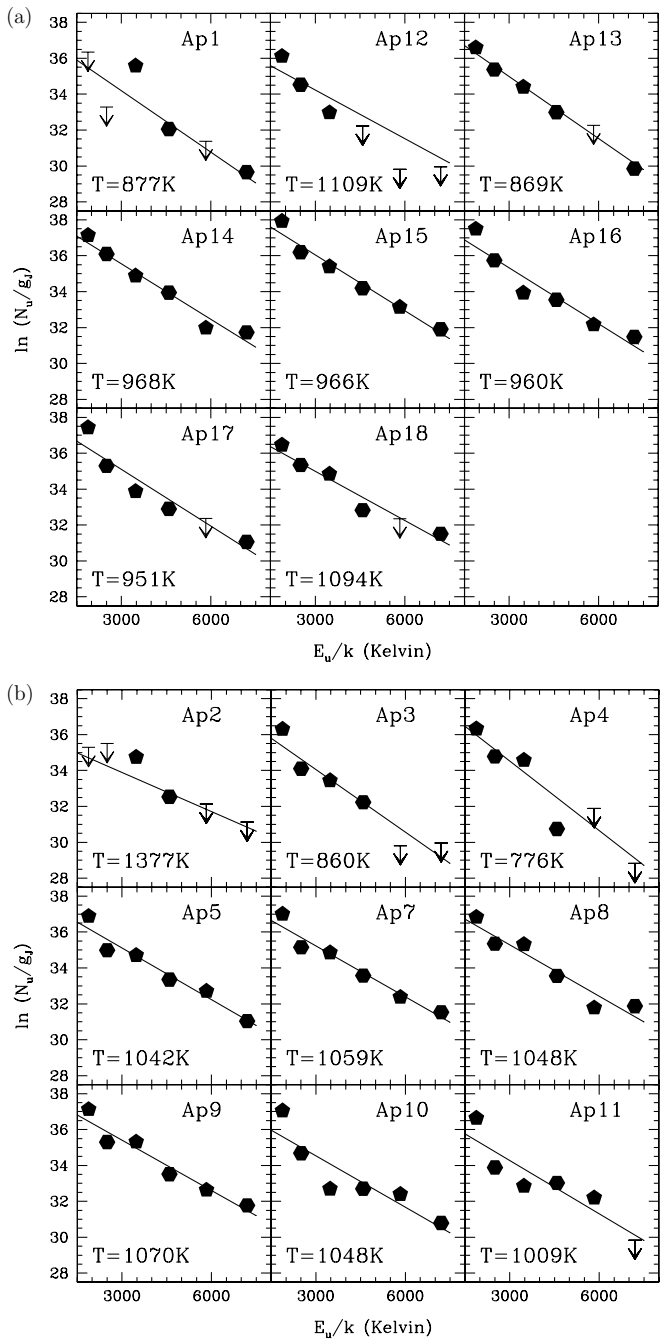

Figure 8. (a) Excitation diagrams as a function of aperture for the protostellar position (Ap1) and in the redshifted outflow lobe of the Wasp-Waist Nebula, moving away from the protostar with increasing aperture number. Solid pentagons indicate *para* transitions; solid hexagons indicate *ortho* transitions. Best-fit straight lines to the data are plotted, and the corresponding derived temperatures are indicated in the bottom left of each panel. (b) Excitation diagrams as a function of aperture in the blueshifted outflow lobe of the Wasp-Waist Nebula, moving away from the protostar with increasing aperture number. Solid pentagons indicate *para* transitions; solid hexagons indicate *ortho* transitions. Best-fit straight lines to the data are plotted, and the corresponding derived temperatures are indicated in the bottom left of each panel.

To be certain that this absorption feature is not spurious, due to improper background subtraction, we examined the image of the SL1 background map (whose position is indicated in red in the top panel of Figure 2), the SL1 map without background subtraction (whose position is indicated in red in the bottom panel of Figure 2), and, finally, the background-subtracted on-source map. We present the background-subtracted, on-source map, integrated over the 10.95–11.76 μm wavelength range, in Figure 9. Note that the 11.3 μm feature appears in *emission* in regions plotted as white toward the map edges. There is also significant variation in the shape of the background continuum absorption and in the depth of the 11.3 μm absorption as a function of position in the protostellar envelope and within the outflow cavity.

4. DISCUSSION

4.1. Flow Morphology: Distinguishing Line Emission from the Scattered Light Nebulosity

One key motivation for spectral mapping of the Wasp-Waist Nebula was to distinguish the outflow's morphology from that of the scattered light nebula and from the ubiquitous relatively high background emission from transiently heated graphitic VSGs and PAHs.

The IRAC images of the Wasp-Waist Nebula are presented in Figure 10. The outflow cavity walls, displaying a beautiful, hourglass shape, are seen in scattered light in the two shortest wavelength IRAC bands, along with any shocked gas features which may be present. IRAC Band 1 (3.6 μm) encompasses six H_2 emission lines, along with the 3.3 μm PAH feature. IRAC Band 2 (4.5 μm) includes seven H_2 emission lines, as well as the Brα line of H I (Smith & Rosen 2005a). The 4.5 μm band, in particular, has been used to identify new candidate outflows from IRAC images (Zhang & Wang 2009; Cyganowski et al. 2008). However, as can be seen by examination of Figure 10, disentangling the scattered light contribution from the shocked line emission based on these images alone is not possible. The confusion between continuum and line emission in the 4.5 μm band image serves as a cautionary note to claiming *any* "extended green object" (EGO) to be exhibiting purely shocked gas emission, in the absence of ancillary data. The unfortunate term, EGO, refers to the common color-coding of IRAC images in which the 4.5 μm band is rendered in green, e.g., Cynagowski et al. (2008).

The IRAC Band 3 (5.8 μm) image starts to show the envelope in absorption surrounding the central protostar, against the VSG and PAH background emission. This IRAC filter encompasses eight H_2 emission lines, as well as the 6.2 μm PAH feature (Smith & Rosen 2005a). The protostellar envelope is dramatically evident in absorption in IRAC Band 4 (8.0 μm). This band includes two strong PAH features: one at 7.7 μm and the other at 8.6 μm, against which the envelope is seen in absorption.

Figure 11 shows the clear separation of shocked, outflow emission from the scattered light of the Wasp-Waist Nebula. Whereas the cavities of the protostellar envelope are hourglass-shaped, the shocked gas exhibits a distinct S-shaped pattern. The result of our IRS spectral mapping of the outflow associated with the Wasp-Waist Nebula is shown in the top panel, which shows the integrated H_2 line intensity map. This latter image was obtained by summing the six H_2 outflow emission maps of Figure 3. The bottom panel of Figure 11 shows the IRAC 3.6 μm image, in which the scattered light cavities are the most prominent. The green contours superposed on the 3.6 μm image show the peaks in the mid-IR H_2 emission. The integrated H_2 line map is distributed in a point-symmetric, S-shape about the central protostellar position.

Protostellar outflows are all bipolar, but vary widely in their detailed morphology. The underlying jets and flows are

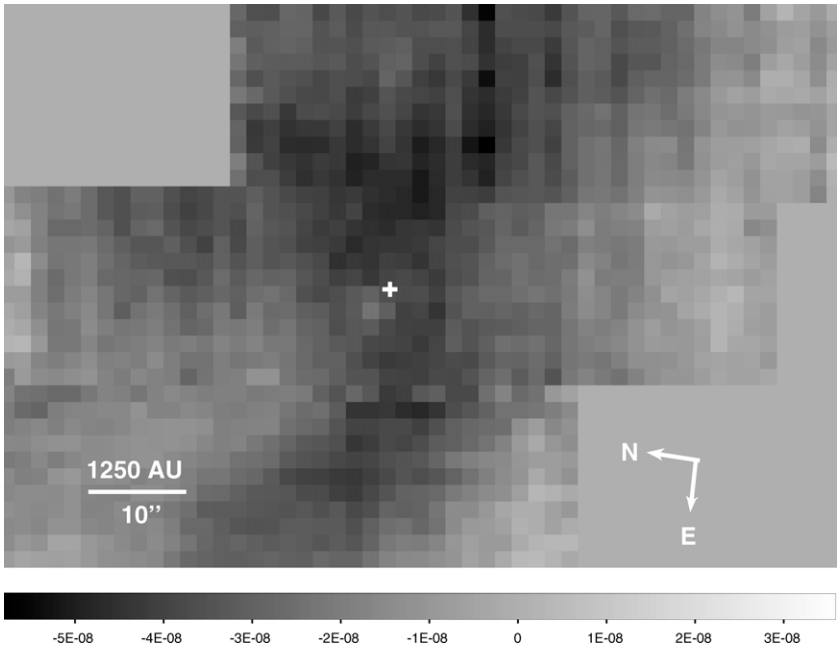

Figure 9. Sky-background subtracted IRS map of the 11.3 μm PAH feature, integrated over the wavelength interval, 10.95 μm $\leqslant \lambda \leqslant$ 11.76 μm. The white cross indicates the 1.1 mm continuum position of the protostar, IRAS 16253−2429 (Stanke et al. 2006). The map shows both emission and absorption. The colorbar is in W m^{-2} sr^{-1} units and goes negative (into absorption) over much of the envelope. Regions of feature emission appear white in this map.

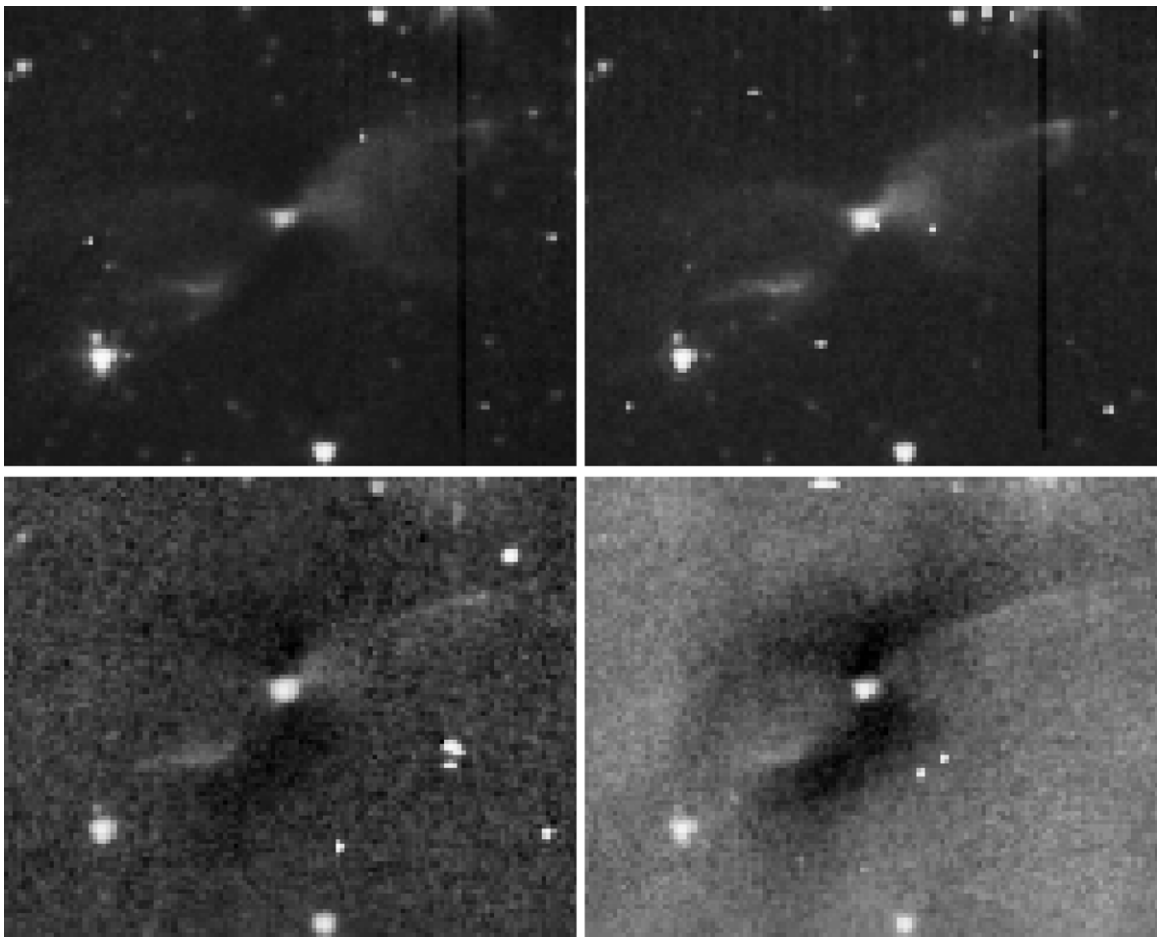

Figure 10. Top panels: IRAC Band 1 (left) and Band 2 (right) images of the Wasp-Waist Nebula. Bottom panels: IRAC Band 3 (left) and Band 4 images.

generally not directly accessible observationally, rather, the underlying jet and/or wind properties are inferred from the shocks they create via their interactions with the surrounding interstellar medium. These shock tracers span a great portion of

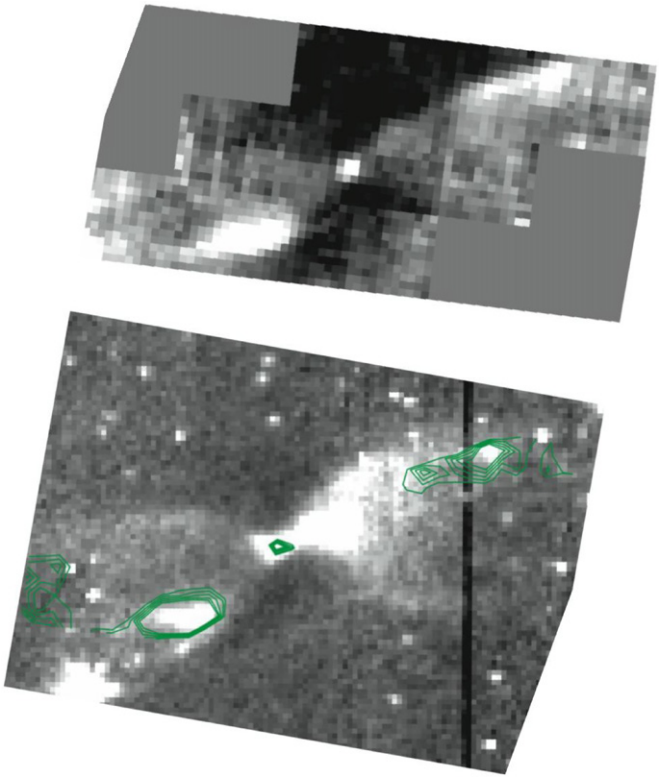

Figure 11. Top panel shows the H_2 emission integrated over the wavelengths of all six H_2 transitions detected by the IRS instrument. Note the prominent S-shaped symmetry about the central source displayed in the H_2 emission map. The continuum absorption envelope is seen even when integrated over the narrow wavelength intervals of the six H_2 emission lines. The bottom panel shows the IRAC 3.6 μm image of the Wasp-Waist Nebula in grayscale. The prominent hour-glass shape from the scattered light-illuminated cavities is clearly seen. (The bright emission toward the bottom left of the image is contamination by a foreground star). The superposed green contours show the locations of the H_2 emitting regions mapped with the IRS instrument. The H_2 emission clearly does not follow the cavity shapes.

(A color version of this figure is available in the online journal.)

the electromagnetic spectrum, depending on the intrinsic nature of the jet/wind (its temperature, density, velocity) and that of the surrounding medium. Observed flow morphologies range from quite wide-angled (e.g., Colgan et al. 2007; Matthews et al. 2010) to terrifically narrow-angled, and highly collimated (e.g., Lee et al. 2007; Codella et al. 2007). Detailed flow morphologies vary, even within the same flow, depending on the tracers used (e.g., H_2, CO, HCO^+, SiO, [S II]), the physical scales observed, and the angular resolution.

Cavities in protostellar envelopes are generally observed in scattered light images at NIR and mid-IR wavelengths for Class I and Class 0 protostars, respectively (e.g., Tamura et al. 1991; Padgett et al. 1999; Ybarra et al. 2006 for the former, Tobin et al. 2007, 2008; Noriega-Crespo et al. 2004; Looney et al. 2007; Gâlfalk & Olofsson 2007 for the latter). In general, the scattered light cavities are all fairly wide-angled, posing a challenge to theories of protostellar jet formation and propagation, in the form of fundamental unanswered questions: is the initial flow an isotropic wind, a poorly collimated jet, a well-collimated jet, or some combination of these? From where is each jet/wind component launched? Under what circumstances will a jet be time variable (pulsed)? Why do some jets appear to precess, and what determines their precession timescales? Do jets widen with time, as some authors have suggested, to disperse their natal cloud cores and end the infall phase (Velusamy & Langer 1998; Arce & Sargent 2005)? These are the motivating questions for separating the outflow and cavity components in the very earliest protostellar stage.

If one believes that fast ($\sim$ a few $\times$ 100 km s^{-1}), highly collimated optical jets and their associated slower ($\sim$ 10–20 km s^{-1}) molecular outflows trace a single phenomenon (Chernin & Masson 1991), then it is still a mystery how a highly collimated, supersonic jet could possibly create the observed wide-angle outflow cavities associated with the vast majority of protostellar flows. In the jet-driven molecular outflow model, jets accelerate the ambient molecular gas through prompt entrainment at bow shocks (Chernin et al. 1994). Could a wandering jet account for the observed wide outflow cavities (Ybarra et al. 2006)?

Hydrodynamic simulations of cavities created by wide-angle winds or jet-driven outflows predict the density structure of the resultant cavities close to the source (Cunningham et al. 2005). Magnetohydrodynamic flows can now be simulated, as well (Cunningham et al. 2009), propagating into inhomogeneous media (Shroyer et al. 2009). The resultant calculated density structures can be used as input to Monte Carlo radiative transfer codes (e.g., Whitney et al. 2003) to compare model cavity shapes calculated for different outflow characteristics with actual, observed cavity shapes. The aim is to directly address the question raised above: is the initial flow an isotropic wind, a poorly collimated jet, or some combination of these?

Further constraints on flow characteristics can be provided by comparing the observed pure H_2 emission maps with model molecular emission-line images. Model H_2 line images can be produced by combining 3-D hydrodynamic jet simulations with chemistry and molecular cooling. A given jet model will generate predicted images of shocked emission in each H_2 line. Hydrodynamic jet models whose physical structures have been computed include jets with time-variable mass-loss rates (Rosen & Smith 2003), continuous or pulsed fast-precessing jets (Rosen & Smith 2004), and slow-precessing jets (Smith & Rosen 2005b) (fast or slow relative to the jet's expansion rate into the external medium).

The above-outlined explorations will be the subject of future papers, for which the separation of the mid-IR reflection nebulosity (produced by scattered light off the cavity walls) from the pure H_2 line emission produced by the currently active outflow, is crucial.

4.2. PAH Feature Emission/Absorption

As noted in Section 3.3, and as can be seen in Figure 9, the 11.3 μm PAH feature is found *in absorption* throughout much of the protostellar envelope in this source. Why is this the first object to be seen in absorption in the 11.3 μm PAH feature?

With the high sensitivity of IRAC aboard *Spitzer*, several Class 0 sources are known to exhibit complex absorption structures in IRAC's Band 4, centered at 8.0 μm (e.g., Looney et al. 2007; Tobin et al. 2010). The absorption in these sources has generally been attributed to absorption against the Galactic mid-infrared background. The same has been assumed for the mid-infrared absorption of the Infrared Dark Clouds, first discovered with the Midcourse Space Experiment (MSX; e.g., Rathborne et al. 2010). Pre-stellar cores have been studied in absorption at $\lambda \sim 7$ μm with *ISO*, and again, the absorption was assumed to be against the Galactic background in that waveband, with the characteristics of general insterstellar dust (Bacmann et al. 2000; Steinacker et al. 2005).

All of the aforementioned observations of mid-infrared absorption were acquired through wide-band continuum filters. To

definitively detect the 11.3 μm feature in absorption requires the spectral resolution of the IRS instrument (or better), and a bright background at this wavelength, against which to absorb. IRS spectra of a few Class 0 protostars are available, notably from the c2d (Cores to Disks) *Spitzer* Legacy program. None of the Class 0 protostars observed in scanning mode are detected below ~20 μm with IRS. The Class 0 sources in Perseus, although detected in the IRAC bands (via scattered light), are not seen in absorption against a bright mid-infrared background (Tobin et al. 2007). The same is the case for the Taurus protostar, L1527 (Tobin et al. 2008). For spectra acquired in stare mode, an off-source position along the slit is often used for background subtraction. Our spectral scan map (Figure 9) shows that the 11.3 μm absorption is spatially extended, making background subtraction from within the slit (or from nearby positions) unreliable.

The physical significance of the detection of PAH-feature absorption in this protostellar envelope is to highlight the importance of including PAHs and VSGs, in addition to the "standard" ISM (interstellar medium) dust used in a variety of computer modeling efforts, since these components are clearly present. The affected modeling efforts include cloud chemistry, shock chemistry, and radiative transfer in protostellar envelopes and disks. In a recent IRS spectral survey of YSO disks, about 3% are found to be PAH emitting (Oliveira et al. 2010). The spatially resolved disk around the Herbig Be star, WL16, in the ρ Oph core, is a well-documented case of a PAH-emitting, pre-main-sequence disk (Ressler & Barsony 2001; DeVito & Hayward 1998). The absence of PAH emission from YSO disks, however, is not necessarily a sign of the absence of PAHs, but, instead, may be due to the absence of available UV photons to excite the PAHs. Interestingly, PAH feature absorption is especially strong right at the protostellar position of IRAS 16253−2429 (see bottom spectra in Figures 5(a) and 5(b)), where scattered light in the IRAC bands is strong. This may mean that the compact disk component surrounding IRAS 16253−2429 likely has PAHs in it, too, even in the absence of PAH emission.

4.3. Excitation Analysis of Shocked Gas

4.3.1. Flow Mass and Luminosity

Mass determinations based on H_2 emission-line measurements are surprisingly rare. Ground-based observations, with few exceptions, generally map the 2.122 μm $v = 1 \rightarrow 0$ $S(1)$ line. Two major problems follow: (1) the extinction to the emitting regions is generally unknown (and variable across the source) and (2) the excitation temperature of the gas is unknown, leaving the determination of the column density to an educated guess. The advantage of space-based platforms, e.g., *ISO* and *Spitzer*, has been the accessibility to mapping the emission in a multitude of H_2 transitions inaccessible from the ground, including the lowest lying (v = 0-0) lines, where most of the H_2 gas mass resides. Such observations allow determinations of the relevant excitation temperatures, and, therefore, of column densities. The *warm* gas mass toward Peak 1 in Orion within an *ISO* aperture is derived to be 0.06 $M_\odot$ ± 0.015$M_\odot$ in this way (Rosenthal et al. 2000). For five Class 0 protostellar flows mapped with *Spitzer* in the eight lowest lying $v = 0 - 0$ transitions, the H_2 gas masses (for $T > 100$ K) are derived to be (Neufeld et al. 2009): 1.3×10^{-3} $M_\odot$ (VLA1623), 2.5×10^{-3} $M_\odot$ (BHR71), 8.1×10^{-3} $M_\odot$ (L1448), 4.9×10^{-2} $M_\odot$ (L1157), and 0.18 $M_\odot$ (NGC2071).

For the IRAS 16253−2429 outflow, the total observed H_2 column density for each aperture is listed in Table 4. For each aperture, the total observed H_2 column density is the sum of the extinction-corrected H_2 column densities of the six observed H_2 transitions. Since each aperture has dimensions of 7.″40 × 7.″40, it is straightforward to calculate the gas mass observed in each outflow lobe:

$$M_{\rm total} = \sum_{\rm Apertures} N_{\rm H_2}\, \mu_G\, m_{\rm H_2}\, d^2 d\Omega, \quad (8)$$

where the summation is over all of the apertures covering each outflow lobe, $m_{\rm H_2}$ is the molecular hydrogen mass, $\mu_G = 1.36$ is the mean atomic weight of the gas (including He), and we have adopted $d = 125$ pc as the distance to the source (Loinard et al. 2008). This gives 1.58 ± 0.04 × 10^{27} g or 7.95 ± 0.19 × 10^{-7} $M_\odot$ for the gas mass in the redshifted outflow lobe, excluding the gas at the protostellar position, and 1.15 ± 0.03 × 10^{27} g or 5.78 ± 0.17 × 10^{-7} $M_\odot$ for the gas mass in the blueshifted outflow lobe. Although some H_2 certainly exists in higher excitation states than what we have mapped here (e.g., the $v = 1 \rightarrow 0$ $S(1)$ H_2 emission line), most of the mass will be found at the lowest energies (viz. Bertoldi et al. 1999; Rosenthal et al. 2000).

It is of interest to compare the derived warm H_2 gas mass with the mass of cold, swept-up gas, traced primarily by millimeter lines of CO. In this context, it is important to bear in mind that estimation of cold gas masses from CO observations is fraught with difficulties. These are the assumed, but uncertain, [CO/H_2] abundance ratio, the line opacity value(s) for the observed CO line, and emission from the ambient cloud that hides the mass in the outflowing gas that appears at low Doppler-shifted velocities. With all of these caveats, the inferred gas mass from CO (3→2) mapping of the IRAS 16253−2429 flow is 1.6×10^{-4} $M_\odot$ for the blueshifted lobe and 8.1×10^{-4} $M_\odot$ for the redshifted lobe from a total mapped area of 80″ × 180″ versus 63″ × 137″ for the IRS map (Stanke et al. 2006). The quoted CO-derived mass values are uncorrected for optical depth and inclination effects, and are, therefore, lower limits. This comparison leads to the inevitable conclusion that, by far, the bulk of the gas associated with the outflow is at quite low temperatures, e.g., 30 K. Recall that the cold CO gas represents swept-up gas associated with the outflow, and, is, therefore, a tracer of outflow activity integrated over the outflow's entire lifetime, in this case a dynamical time of $t_{\rm dyn} = 1.5 \times 10^4$ yr. In contrast, the cooling time of the hot H_2 gas we have mapped with IRS is on the order of years, so, essentially, giving us a snapshot view of current outflow activity.

The extinction-corrected line luminosities, summed over all six observed H_2 transitions, seen through each aperture with their corresponding errors are listed in Column 4 of Table 4. The radiated luminosity from each lobe is then easily calculated by summing the contributions from all of the apertures within each lobe. In this way, the calculated emission-line luminosity in the redshifted lobe is 7.46 ± 0.19 × 10^{28} erg s^{-1} or 1.94 ± 0.05 × 10^{-5} $L_\odot$ and 7.13 ± 0.15 × 10^{28} erg s^{-1} or 1.86 ± 0.04 × 10^{-5} $L_\odot$ in the blueshifted lobe. These values can be compared with the mechanical luminosities in each lobe derived from the CO data: 4.9 (92) × 10^{-5} $L_\odot$ for the redshifted lobe and 1.0 (19) × 10^{-5} $L_\odot$ for the blueshifted lobe, where the values in parentheses have been corrected for optical depth and inclination effects (Stanke et al. 2006).

Table 4
Wasp-Waist Nebula Outflow: Derived Physical Properties

Position in Flow	Aperture Number[a]	N_{H_2}[b] (10^{16} cm^{-2})	L[c] (10^{27} erg s^{-1})	T_{kin}[d] (K)
Protostellar Position	1	4.11 ± 0.65	5.11 ± 0.86	877
Blueshifted Outflow Lobe	2	2.21 ± 0.32	3.15 ± 0.35	1377
...	3	8.29 ± 1.38	2.60 ± 0.26	860
...	4	11.1 ± 1.12	3.27 ± 0.33	776
...	5	18.0 ± 1.63	10.8 ± 0.46	1042 ± 103
...	7	20.7 ± 0.78	13.0 ± 0.55	1059 ± 103
...	8	21.4 ± 1.25	15.0 ± 0.58	1048 ± 146
...	9	24.1 ± 1.26	15.3 ± 0.61	1070 ± 117
...	10	16.1 ± 1.87	6.55 ± 0.84	1048 ± 240
...	11	10.5 ± 1.21	4.74 ± 0.43	1009
Redshifted Outflow Lobe	12	8.69 ± 1.39	2.35 ± 0.48	1109
...	13	16.8 ± 1.45	7.00 ± 0.47	869
...	14	32.7 ± 2.25	18.4 ± 0.90	968 ± 88
...	15	51.1 ± 2.05	25.3 ± 0.96	966 ± 72
...	16	31.1 ± 1.25	13.4 ± 0.53	960 ± 133
...	17	25.1 ± 1.85	8.1 ± 0.55	951
...	18	16.4 ± 0.86	9.6 ± 0.81	1094

Notes.
[a] Aperture positions are as listed in Table 1 and as shown in Figure 4.
[b] Extinction-corrected and summed over the six observed transitions of Table 1.
[c] H_2 line luminosity, extinction-corrected, and summed over the six observed transitions of Table 1.
[d] All tabulated values correspond to the straight line fits plotted in Figure 8. Errors could only be determined for apertures in which all six transitions were detected.

4.3.2. Flow Kinetic Temperature

Figure 8(a) shows the excitation diagrams, as a function of aperture, for the protostellar position (Aperture 1) and for positions along the redshifted outflow lobe (Apertures 12–18), in order of increasing distance from the protostellar position. The temperatures derived from the best-fit slopes of the straight lines fitted to the plotted data points are indicated in each panel and are tabulated in the last column of Table 4. For apertures through which all six H_2 transitions were detected (Apertures 14–16 in the redshifted outflow lobe) straight line fits to the data pass the F statistic test at the 95% confidence level, indicating that a fit to a straight line (as opposed to a higher order curve) is justified. The resultant uncertainties in the derived temperatures for the gas observed through these apertures are also tabulated in Column 5 of Table 4. The temperatures through these apertures show a remarkable constancy: all are in the range $T = 950$–970 K.

Figure 8(b) shows the excitation diagrams, as a function of aperture, for positions moving away from the protostar in the blueshifted outflow lobe. For apertures through which all six H_2 transitions were detected (Apertures 5–10 in the blueshifted outflow lobe), again, straight line fits to the data in these apertures pass the F statistic test at the 95% confidence level, indicating that a fit to a straight line (as opposed to a higher order curve) is justified. The temperatures derived from the best-fit slopes of the straight lines fitted to the plotted data points for Apertures 5–10 are also remarkably constant and fall in the range $T = 1042$–1070 K.

In summary, the temperatures derived from the excitation diagrams through apertures in which all six H_2 transitions were detected, show remarkable constancy along the observed shocked features: all are ∼1000 K within the errors. For reference, the derived temperatures for each aperture are listed in the last column of Table 4. Uncertainties in the slopes of the fitted lines, and, therefore, in the derived temperatures, could be determined only for apertures in which all six H_2 transitions were detected. These errors are listed in Column 5 of Table 4. The fact that the data points for each excitation plot are consistent with straight line fits, as opposed to showing evidence of curvature, means that the observed gas is in LTE—that is to say, the level populations follow a Boltzmann distribution for the derived temperatures.

One may naïvely have expected the flow kinetic temperature to decrease as one gets progressively further from the source (as has been found in a few positions in the L1448 flow by Dionatos et al. 2009). This behavior would be expected if one were observing the actual jet material. Alternatively, one may have found a gradual increase in kinetic temperature, signalling re-acceleration further out along the flow lobes. The relatively constant temperatures observed as a function of distance from the protostar along the outflow lobes in the strongest H_2 emitting features signal similar shock conditions over relatively large areas (20″–30″ or 2500–3750 AU) of the flow.

4.3.3. Ortho/Para Ratios, Shock Models, and Thermal History of the Gas

In the excitation diagrams of Figure 8, *ortho* transitions are plotted as solid hexagons and *para* transitions as solid pentagons. We find no systematic difference using just the *ortho* transitions or the *para* transitions in the inferred temperatures through any of our apertures. As noted above, from the goodness of the straight-line fits to the excitation diagrams displayed in Figure 8, the emitting gas is in LTE at high temperatures (∼900–1000 K). The equilibrium *ortho*/*para* ratio (*opr*) for gas at this temperature, and, indeed, for gas with $T > 300$ K, is 3:1 (see Equation (1) of Kristensen et al. 2007, for example, for the definition of equilibrium *opr* for H_2).

In the interstellar medium, molecular hydrogen must form on grain surfaces. In cold, pre-stellar cores, and in the interiors of giant molecular clouds shielded from UV radiation, the dust grains are covered with ice. Since water is the most

abundant molecule in the solid phase in these environments (Dartois 2005), dust grain surfaces are mainly covered with amorphous water ice. Under these cold conditions, H_2 forms in its lowest electronic state, which, because of the nuclear spins of its identical constituents, exists in two varieties: *para*-H_2, with even J rotational quantum numbers, and *ortho*-H_2, with odd J rotational quantum numbers. It turns out that there is a small (∼2.6 meV, corresponding to ∼30 K), but important, difference in the adsorption energy of *ortho*-H_2 versus *para*-H_2 onto such surfaces, in the sense that the *ortho* variety of H_2 tends to stick more than the *para* variety (Buch & Devlin 1994). Such a difference in adsorption energies for *para* and *ortho* forms to an amorphous water–ice substrate has been experimentally observed just recently for D_2 (Amiaud et al. 2008). This phenomenon is explained qualitatively in the following way: the wavefunction of *para*-H_2 ($J = 0$) is approximately spherically symmetric, resembling an H atom's s electronic wavefunction, whereas the wavefunction of *ortho*-H_2 ($J = 1$) is similar to the non-spherical H-atom's p electronic wavefunction. This results in *para*-H_2 being impervious to anisotropies in the grain surface's energy potential, in contrast to *ortho*-H_2, which, due to its own anisotropy, binds more strongly. Thus, for thermal desorption of H_2 from grain surfaces at temperatures, $T \leqslant 30$ K, the H_2 gas is almost exclusively in its *para*-H_2 form.

Another mechanism favoring a low *opr* is the proton exchange reaction (Flower & Watt 1984, 1985):

$$H_2(ortho) + H^+ \rightleftharpoons H_2(para) + H^+ + 170.5\,\mathrm{K}, \quad (9)$$

where the energy given off is just the energy difference between the $J = 1$ and $J = 0$ pure rotational states.

These authors found that for a cosmic-ray ionization rate, $\zeta = 10^{-17}$ s^{-1}, the timescale, τ, for the *opr* to reach 0.01 through this mechanism is $\approx 10^6$ yr for clouds in which 10^2 cm^{-3} $\lesssim n(H_2) \lesssim 10^3$ cm^{-3}, but an order of magnitude longer, $\tau \approx 10^7$ yr, for dense clouds in which 10^4 cm^{-3} $\lesssim n(H_2) \lesssim 10^5$ cm^{-3}. This difference in timescales stems from the available proton density. In diffuse clouds, photoprocesses maintain a relatively high proton density, whereas in denser clouds, photoprocesses are minimized and the proton density is further reduced by charge exchange processes with neutral molecules. Ironically, the initial *opr* from formation on grains assumed for the above calculations was 3:1.

The question then becomes how H_2 attains the observed *opr* of 3:1, or any *opr* $\geqslant$0.01, for that matter? The answer lies in shock heating and chemistry. An important mechanism for interconverting between *para*-H_2 and *ortho*-H_2 is that of chemically reactive collisions with neutral hydrogen atoms

$$H_2(para) + H + 3900\,\mathrm{K} \rightleftharpoons H_2(ortho) + H. \quad (10)$$

Although the 3900 K barrier to reactive scattering of H+H_2 to produce *ortho*-H_2 from *para*-H_2 is substantial (Schofield 1967; Siegbahn & Liu 1978; Park & Light 1989), this barrier can be overcome for $T > 1000$ K, temperatures attainable in shocks (Le Bourlot et al. 1999).

In previous studies of H_2 in protostellar outflows, *opr* values have been found to vary: values of $0.2 \leqslant opr \leqslant 2$ have been found in NGC1333, HH54, and HH7-11 (Maret et al. 2009; Neufeld et al. 2006). However, *opr* values of 3 have been observed toward outflows in Orion and L1448 (Rosenthal et al. 2000; Dionatos et al. 2009). In the context of these H_2 studies of protostellar flows, the IRAS 16253−2429 flow has the lowest luminosity, by orders of magnitude (see Section 4.3.1).

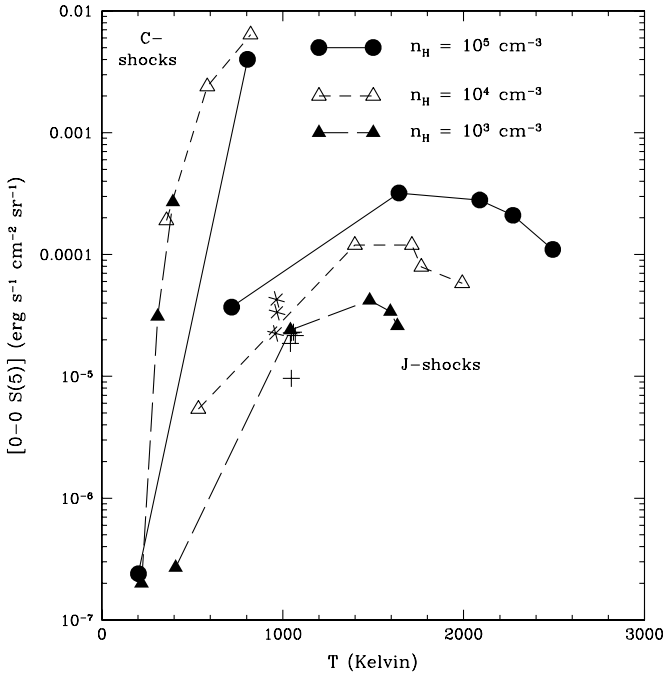

Figure 12. 6.9 μm H_2 line intensity vs. temperature plot. Skeletal stars represent data from Apertures 14–16 in the redshifted lobe; crosses represent data from Apertures 5, 7, 8–10 in the blueshifted lobe. Shock models, with $opr_i = 3$, are from Wilgenbus et al. (2000). Both C-shock and J-shock models are plotted. Each model point (filled triangles, for $n_H = 10^3$ cm^{-3}, open triangles for $n_H = 10^4$ cm^{-3}, and filled circles, for $n_H = 10^5$ cm^{-3}) corresponds to a specific shock velocity. From lower left to upper right, for the C-shock models: $v_s = 20$ km s^{-1}, 30 km s^{-1}, and 40 km s^{-1}, except for the $n_H = 10^5$ cm^{-3} case, for which the plotted points are for $v_s = 20$ km s^{-1} and 30 km s^{-1}. From lower left to upper right, for the J-shock models: $v_s = 5$ km s^{-1}, 10 km s^{-1}, 15 km s^{-1}, 20 km s^{-1}, and 25 km s^{-1}.

In Figure 12, we plot the 6.9 μm H_2 line intensities (from Column 4 of Table 3, extinction-corrected using the 6.9 μm extinction values from Column 6 of Table 3) versus the best-fit temperatures (last column of Table 4). This figure is analogous to Figure 6 of Wilgenbus et al. (2000), for the purposes of comparing shock models with our observations. Data points are plotted only for apertures through which all six H_2 transitions were reliably detected. These are the apertures with well-determined errors in $T_{\rm kin}$, listed in the last column of Table 4. The spatial locations of these apertures within the flow lobes are shown in Figure 4. Our data are represented by skeletal stars for apertures located in the redshifted outflow lobe and by crosses for apertures located in the blueshifted lobe.

The calculated models are for four different initial values of the *opr*, opr_i: 0.01, 1.0, 2.0, and 3.0. Only the models with $opr_i = 3.0$ were consistent with the observed *opr* of 3:1 through each of our apertures, therefore, the models plotted in Figure 12 all have $opr_i = 3.0$. Models with lower starting *opr* never reach final *opr* values of 3:1. From this, we may surmise that previous shock passages are required to have raised the "initial" *opr* of the ambient gas.

The ordinate of Figure 12 is the 6.9 μm line intensity, whereas the abscissa is the temperature inferred from the pure H_2 rotational lines—those accessible with *ISOCAM* for the model points, those derived from *Spitzer's* IRS SL1+SL2 modules for our data points. Plotted curves are of C-shock and J-shock models propagating into media of three different densities, $n_H = 10^3$ cm^{-3}, 10^4 cm^{-3}, and 10^5 cm^{-3}. These "curves" connect computed model points calculated for various shock velocities. The plotted model points for the C-shock case, in order from

lower left to upper right, are for $v_s = 20$ km s^{-1}, 30 km s^{-1}, and 40 km s^{-1}, except for the $n_H = 10^5$ cm^{-3} case, for which the plotted points are for $v_s = 20$ km s^{-1} and 30 km s^{-1} only. Plotted model points for the J-shock case, in order from lower left to upper right, are for shock velocities, $v_s = 5$ km s^{-1}, 10 km s^{-1}, 15 km s^{-1}, 20 km s^{-1}, and 25 km s^{-1}.

The Continuous (C)-type shock wave requires a relatively high transverse magnetic field (100 μG–1 mG). In a C-shock, the ionized and neutral species behave dynamically differently: first, the ionized material decelerates, responding to the magnetic field, and subsequently, this ionized material decelerates the neutral material via collisions, heating the neutrals in the process. For C-shocks, the shock thickness is broad, the deceleration is more gradual than in J-shocks, and, consequently, the temperatures reached are lower than for J-shocks. This is evident in Figure 12, in which the C-shock models are all at lower temperatures than the corresponding J-shocks.

In a Jump (J)-type shock, the gas undergoes a sharp increase in temperature and a dramatic drop in velocity over a few mean free paths. This accounts for the generally higher temperatures attained in the J-shock models. Rapid cooling and compression follow, resulting in the predicted low 6.9 μm line intensities, relative to the C-shock models.

Our data are clearly incompatible with the C-shock models. In general, the C-shock models over-predict the 6.9 μm line intensities by orders of magnitude over what is observed for the relevant temperatures. Our data are well fitted by the J-shock models, however, being fairly tightly clustered in the J-shock regime of the diagram. Furthermore, for the J-shock models, the data for the redshifted lobe lie in the range 10^4 cm^{-3} $\leqslant n_H \leqslant$ 10^5 cm^{-3}, whereas the blueshifted lobe data lie in the range of $n_H \leqslant 10^3$ cm^{-3}. The inferred shock velocity for the redshifted gas lies in the range: 5 km s^{-1} $\leqslant v_s \leqslant$ 10 km s^{-1}, whereas inferred the shock velocity for the blueshifted gas is $v_s =$ 10 km s^{-1}.

Although the models are for J-shocks, some initial magnetic field strength is used as input for all of the models. For the shock velocities in the redshifted lobe, the initial transverse (i.e., perpendicular to the direction of shock propagation) magnetic field strength of 10 μG is used for the $n_H = 10^4$ cm^{-3} case, and a 31.5 μG field strength for the denser, $n_H = 10^5$ cm^{-3}, model. For the blueshifted lobe, with $v_s = 10$ km s^{-1}, and densities $n_H \leqslant 10^3$ cm^{-3}, a weaker initial transverse magnetic field, 3.2 μG, is used by the models. To repeat, the magnitude of the magnetic field component transverse to the shock in the blueshifted lobe is $\sim$3 μG, whereas it is 10–32 μG in the redshifted lobe. These values are the best determination of the ambient magnetic field strengths toward this region. Shock modeling of the H_2 lines in outflows has been suggested as an alternative method to Zeeman-splitting and polarization studies for estimation of the magnetic field strengths in dense clouds (Cabrit et al. 2004), as is demonstrated here.

5. SUMMARY AND CONCLUSIONS

1. A spectral scan map of a 137″ × 63″ area of the Wasp-Waist Nebula associated with the Class 0 protostar, IRAS16253−2429, was acquired with the IRS instrument aboard the *Spitzer Space Telescope* on 2007 March 19. The Short-Low (SL) modules were used, covering the 5.2–14.7 μm wavelength range at low resolution, $\lambda/\Delta\lambda =$ 64–128.
2. The outflow was detected in all six pure rotational H_2 transitions (0-0 $S(2)$–0-0 $S(7)$) that fall within the observed wavelength range. Outflow maps are presented for each detected H_2 transition. The outflow structure is point symmetric about the central protostar, and exhibits an S-shape, in all six line maps.
3. The outflow morphology contrasts with the scattered light appearance of the Wasp-Waist Nebula, most clearly seen at the shortest IRAC bands (3.6 μm and 4.5 μm), which exhibits a bipolar, symmetric, hourglass shape.
4. The protostellar envelope of the Class 0 object, IRAS 16253−2429, is mapped in absorption in the 11.3 μm PAH feature. This is the first instance of a source seen in 11.3 μm PAH absorption.
5. Spatially resolved spectra, as a function of position along each outflow lobe, are presented. Spatially resolved extinctions, through apertures matching the ones through which spectra were extracted were determined using a $\tau_{8\,\mu m}$ map derived from archival IRAC imaging. Excitation diagrams, as a function of position along each outflow lobe, are presented. Temperatures derived from the excitation diagrams through apertures in which all six H_2 transitions were detected show remarkable constancy along the observed shocked features: $T \sim 960$ K in the redshifted lobe and $T \sim 1050$ K in the blueshifted lobe.
6. The total mass of hot ($T \sim 1000$ K) H_2 gas within the mapped area is found to be $7.95 \pm 0.19 \times 10^{-7}$ $M_\odot$ in the redshifted lobe and $5.78 \pm 0.17 \times 10^{-7}$ $M_\odot$ in the blueshifted lobe. These values are a small fraction, of order 10^{-3}, of the cold ($T \sim 30$ K) gas mass derived from CO(3→2) observations (Stanke et al. 2006).
7. The total luminosity radiated in the pure rotational H_2 lines approaches the total mechanical luminosity of each outflow lobe. Specifically, the emission-line luminosity, integrated over all observed transitions, over all of the apertures in the redshifted lobe, is $7.46 \pm 0.19 \times 10^{28}$ erg s^{-1} or $1.94 \pm 0.05 \times 10^{-5}$ $L_\odot$. The analogous value in the blueshifted lobe is $7.13 \pm 0.15 \times 10^{28}$ erg s^{-1} or $1.86 \pm 0.04 \times 10^{-5}$ $L_\odot$.
8. A value of 3:1 for the H_2 *opr* is found for the emitting gas through all apertures along both the red- and blueshifted outflow lobes. This finding suggests that previous shock passages must have occurred to drive the observed H_2 *opr* to such a high value.
9. Detailed comparison of the H_2 data presented here with the shock models of Wilgenbus et al. (2000) is consistent with the emitting gas passing through Jump (J-type) shocks in both outflow lobes. For the redshifted lobe, the inferred shock velocities are in the range 5 km s^{-1} $\leqslant$ v_s $\leqslant$ 10 km s^{-1} and pre-shock densities in the range 10^4 cm^{-3} $\leqslant$ n_H $\leqslant 10^5$ cm^{-3}. For the blueshifted lobe, $n_H \leqslant 10^3$ cm^{-3} and $v_s = 10$ km s^{-1}. The initial transverse magnetic field strength is 3.2 μG for the blueshifted lobe and in the range 10–32 μG for the redshifted lobe.
10. A cookbook for the Cube Builder for IRS Spectral Mapping (CUBISM) software used to analyze the IRS Spectral Mapping data (Smith et al. 2007) is presented in the Appendix.

We are grateful to the scientific team that contributed to the successful *Spitzer* GO Cycle 3 proposal leading to the observations reported here, in alphabetical order: Hector Arce, David Cole, Angela Cotera, Adam Frank, Dirk Froebrich, Alyssa Goodman, Karl Haisch, Jr., Robert Hurt, Gerald Moriarty-Schieven, Randy Phelps, Mike Ressler, Raghvendra Sahai, Janet

Simpson, M. D. Smith, and Jason Ybarra, and to Sean Carey who first suggested this project. We thank Tom Jarrett and Phil Appleton who advised us on data-taking strategy in order to avoid chip saturation through the peak-up arrays by the high zodiacal background toward our target. We also thank the Spitzer Science Center staff who took the data and developed the IRS data reduction pipeline. We especially thank the SSC teams that put on the Data Reduction Workshops and peopled the Help Desk. J. D. Smith and the team who provided the contributed CUBISM software are gratefully acknowledged. We are indebted to Patricia Monger and Robert Lupton, who have provided the SM plotting software and its documentation. This research has made use of SAOImage DS9, developed by Smithsonian Astrophysical Observatory; of NASA's Astrophysics Data System (ADS) bibliographic services, and of the SIMBAD database, operated at CDS, Strasbourg, France. This work is based on observations made with the *Spitzer Space Telescope*, which is operated by the Jet Propulsion Laboratory, California Institute of Technology under a contract with NASA. Support for this work was provided by NASA through an award issued by JPL/Caltech. G.W.-C. and M.B. thank the Brinson Foundation for generous travel support necessary for the completion of this project and for providing funds to help cover publication costs. The anonymous referee whose suggestions improved the paper enormously is gratefully acknowledged.

APPENDIX

CUBISM COOKBOOK

A very useful and beautifully implemented software package, CUBISM (the Cube Builder for IRS Spectral Mapping, Smith et al. 2007) was used for the reduction and analysis of the spectral line maps presented in this work. Although a CUBISM User Manual (Edition 1.7, 2009 July) is available for downloading from the Spitzer Science Center, http://ssc.spitzer.caltech.edu/dataanalysistools/tools/cubism, a short synopsis of a typical data analysis workflow is presented here, as it may prove helpful for other workers in the field.

1. Load Your IRS Basic Calibrated Data (BCD) into CUBISM
   Have your IRS data available on disk. It is fine to keep the same directory structure as is created by the Leopard Data Archive downloading software. For our case, the BCD data are all contained in a single directory (BCD_17Aug07), which is, itself, organized into six subdirectories, corresponding to the six AORs executed to obtain our maps, and renamed, for clarity: SL1-Center (AOR 19062528), SL1-Offset2 (AOR 19062784), SL1-Offset3 (AOR 19063040), SL2-Center (AOR 19063296), SL2-Offset2 (AOR 19063552), and SL2-Offset3 (AOR 19063808). Start CUBISM on your system. A window asking you to load your Cube Project appears. You can then navigate to the directory which contains your BCD data. Alternatively, you can start CUBISM from within your data directory.
   (a) Create a New "Cube Project"
   Click on the bottom bar in the window, labeled "Create New Cube Project." You are then prompted for a project name, which is just a title that will always appear on the title bar of your CUBISM Project window. This name is distinct from any .cpj (CUBISM project files) that you can save later. Only three radio buttons at the bottom of the Cube Project window will be enabled: Import AOR (=Astronomical Observing Request), Save, and Close. Click on "Import AOR" and a "Select BCD AOR Directory" window will pop up, displaying your directory/sub-directory tree structure. Choose the highest level directory which contains, within its subdirectories, all of the data you would like to load into CUBISM. CUBISM will search the directory tree for the files it needs to load. CAVEAT: you can only work with a single IRS module at a time for each distinct CUBISM project (e.g., SL1 or SL2). However, as in our case, if you took dedicated background data with SL1 off-source simultaneously with on-source SL2 data, you will need to load the AORs containing the SL1 background data, as well. Click the "Import AOR" button, and an "Add AORs: Your Project Name" pop-up window appears, informing you of the number of data files that the directory you selected contains (1760 in our case). You are asked whether or not you wish to continue. Hitting the "Yes" radio button will result in CUBISM finding all of the BCD files within your directory tree. Once the files are located a new pop-up window, entitled "Load Group" appears, which prompts you to "Choose BCD Data" from among the relevant AORs. The title, module, number of files, total map points (spatial columns × rows × no. of integrations/map point), and total on-source integration times per map point are all displayed. Click on the gray box to the left of each displayed AOR to select it for loading into CUBISM, click on the OK radio button at the bottom of the pop-up window and proceed. Next, the "IRS Calibration" pop-up window appears, stating the default (set of) calibration file(s) loaded by CUBISM. Should you wish to use other than the default calibration files bundled with the CUBISM software, consult the CUBISM manual (p. 46 of the 2008 November edition) on how to proceed. Click the "OK" radio button and your data are (finally) loaded into CUBISM. Filenames and attributes of each data collection event (DCE) file now appear in your CUBISM Project window.
   (b) Re-Open a Previously Saved "Cube Project"
   The "Load Cube Project" window prompts you for the previously saved Cube Project Filename, in our case we had two Cube Projects, "irs_sl1.cpj" and "irs_sl2.cpj," for the SL1 and SL2 data, respectively. For illustrative purposes, assume we chose the irs_sl2.cpj file for CUBISM to open. Just highlight the filename, "irs_sl2.cpj," that appears in the pop-up window (or navigate over to it, in case the file is located elsewhere), and click on the "OK" radio button at the bottom. The CUBISM Project window now appears, in this case with the title, "IRS_SL2," and the filename, "irs_sl2.cpj," enclosed in single brackets. All of the SL1-centered files have horizontal dashes between the displayed columns, indicating that they are "disabled" files.
2. Specify and Load the Background Files
   (a) For a New "Cube Project"
   As previously mentioned, half the data acquired for each of our SL1-centered maps served as sky background for the SL2-centered maps, and vice versa (see Figure 2). For illustrative purposes, assume we are

working with the SL2 data for our CUBISM project, but have loaded all of our AORs, which include both SL2-centered data along with SL1 sky background measurements. You need to disable the SL1-centered files so they will be excluded from the SL2 Cube you will be building in the next step. This is done in the CUBISM project window, by first selecting the (880 files, in our case) SL1-centered data (by holding down the mouse button as you scroll down the list in the CUBISM Project window—this highlights, or selects, the desired files) and subsequently clicking on the Disable radio button at the bottom of the CUBISM Project window. (Disabled files are indicated by dashed lines appearing between the informational columns for each DCE file in the CUBISM Project window.) Next, you must set the background before building the cube. In order to do this, you must first select all of the background records from within the CUBISM Project window (again, by holding down the mouse key as you scroll down the list of files). Then, when all of the relevant records you would like to use for your background have been highlighted (i.e., selected) hit the Background button at the top of the CUBISM Project window and select: "Set Background from Records." A pop-up window, entitled "Set BCD Background" appears, with two choices: Average or Average + Min/Max Trim. Pick the second choice by clicking on the gray diamond to its left. (CAVEAT: the selected choice is the one with the darker gray shading in the diamond to its left, despite the fact that a black box automatically outlines the first choice. The location of this black box frame around "Average" (the first choice) is irrelevant)! Once you have made your selection, click the OK radio button at the bottom of the pop-up window. To save this list of background records into a file (so you will not have to re-specify them again), from the Background menu item, scroll down to "Save Background Recs." A pop-up window, "Save Background List As..." appears, showing the active directory and allowing you to choose the directory to save the background records list to, and to name the file. The extension for the background list file is "bgl."

(b) For a Previously Saved "Cube Project"

An extremely useful radio button at the top of the CUBISM Project Window is the "Info" button. Clicking it gives you the following pull-down menu options: Project Parameters..., As-Built Parameters..., Calibration Set Details..., and Debug Cubism. At this stage, we would like to find out what our current "Project Parameters" are, so clicking on that menu item brings up a window entitled: "IRS_SL2: Parameters." The first line of this informational pop-up window tells us: "IRS Spectral Cube: IRS_SL2 (needs rebuilding)." NB: despite the fact that you have saved your "Cube Project" file, each time you re-enter CUBISM, you must rebuild your cube. The second line tells us the cube size in pixels: $72 \times 34 \times 77$ (in wavelength) and gives the map center coordinates (α_{2000} $16^{\rm h}28^{\rm m}$ $21\overset{\rm s}{.}46$, δ_{2000} $-24^\circ36'28\overset{''}{.}5$, in our case). The third line tells us SL Order 2 has 880 BCDs. The fourth line tells us about the calibration files used and informs us these are currently not loaded. The fifth line tells us that the background consists of 880 records (since we have previously saved the background into a ".bgl" file, as described in 2. (a) above). Therefore, CUBISM already knows what our specified background will be when it re-builds the cube.

3. Build the Cube

(a) For a New "Cube Project"

Under the Cube menu item in the top row of the available menu items in the CUBISM Project window, scroll down to "Set Cube Build Order," and make sure it is set to the correct value (1, 2, 3 for SL1, SL2, or SL3, respectively). CAVEAT: 1 is the default. Deselect your disabled background records (from the previous step above) first, by simply clicking on any one of them within the CUBISM Project window's listing of your data files. This will un-highlight your background records. You are now ready to build your cube for the first time: Choose "Build Cube" under the Cube menu item in the top row of the available menu items in the CUBISM Project window, or simply click on the Build Cube button at the bottom of the same window. Once your cube is built, you can save your project to a CUBISM project file, by scrolling down to the "Save" option under the File menu item in the top row of the CUBISM Project window. You will be prompted as to where to save the file and what to call it in the "Save Cube Project As..." pop-up window. The extension for cube project files is "cpj."

(b) For a Previously Saved "Cube Project"

Hitting the "Info" radio button at the top of the CUBISM Project Window also tells us that CUBISM knows about global and record level bad pixels flagged by the SSC's pipeline processing, but it is unaware of subsequently flagged bad pixels, whether generated automatically or via the Bad Pixel Backtracking Tool, although these had been saved previously to a Bad Pixel file, in this case: "irs_sl2.bpl" (see Section 4 below for creating Bad Pixel, or ".bpl" files for the first time). For now, simply hit the "Build Cube" radio button at the bottom of the CUBISM Project window to re-build our previously saved cube project, with its appropriate background and pipeline-generated bad pixel files. Be patient, it takes a while to build the cube. Once the status line toward the bottom of the CUBISM Project window indicates "Building $72 \times 34 \times 77$ (in our case) cube: done," you should check the Info → As-built parameters, which will now show the calibration files to have been loaded (on the fourth line) and will also show the number of background records used and when these were last generated. Now is the time to load your previously generated Bad Pixel File and re-build the cube. You do this by choosing the "BadPix" menu item from the CUBISM Project window, choosing "Load and Append Bad Pixels" which brings up a pop-up window that allows you to navigate to the desired Bad Pixel File, "irs_sl2.bpl," in our case. (NB: the "Load Bad Pixels" button would replace any bad pixels already set by those specified in your designated Bad Pixel File, whereas the "Load and Append Bad Pixels" button appends the bad pixels designated in your Bad Pixel File to those already set.) Click the "OK" radio button toward the bottom of this pop-up window, and you will note that the "Build

Cube" radio button along the bottom of the CUBISM Project window has changed to "QuickBuild." Click on the "QuickBuild" radio button. The cube is now re-built with your bad pixels flagged according to your Bad Pixel file (in addition to the pipeline flagged bad pixels).

4. Clean Up Your Data

(a) Edge Effects

Many bad pixels populate the edges of the field of view of each slit, so it is best to edit these out. In order to do this, you first need to view the appearance of some of your (representative) data on the chip, along with the slit illumination pattern and the locations of the data from the peak-up cameras.

After the cube is built, choose all of the data collection events (DCEs) for one exposure of one map position, for example, by highlighting these in the CUBISM Project window. For concreteness, let us choose 13 Samples Up the Ramp (SURs) for position 0[1,1] at the central map position, by highlighting these DCEs using the mouse. Once you have selected these DCEs to display, click on the "View Stack" radio button at the bottom of the CUBISM Project window.

This will bring up a CubeView window, entitled, "CubeView; IRS_SL2 <Average of 13 recs>" in our case. You will now see the entire chip and the illumination pattern of the chip by the Peak-up Cameras (the two rectangular apertures displayed on the right) as well as the SL1, SL2, and SL3 orders. Use the "Scale Image with Histogram" tool (2nd icon of the menu icons in CubeView) to set the grayscale of the display. Proper scaling, in this context, will reveal the bad pixel edges of the slit pseudo-rectangle(s) projected on the chip. This is referred to, in Spitzer-ese, as the "WaveSamp" window (or WS for short). The default is 0.00→0.00:1.00→1.00. Play around with these limits until most of the edge-effect bad pixels are excluded. You do this by clicking the box (making it dark instead of light gray) next to "Show." A rectangular outline with lines across it, all in purple, will appear. Then when you highlight (turn from light to dark gray by clicking on it) the box next to Edit, 6 "handles" = little purple diamonds will appear. You can then use the mouse to click and drag any of these "handles" to exclude the offending edge pixels.

For our SL2 data, 0.03→0.03 and 0.96→0.96 for the pseudo-rectangle aperture looks good. Implement this for the entire cube by re-building the cube. Under the Cube menu item in the top line of the CUBISM Project window, the very last choice is aperture. Right now, for us it reads Ord 2 0.03→0.96. Click OK, this is what you want. Now, rebuild the cube. When you save your work to a "Cube Project" (.cpj file) this information will be saved as well, so you will not need to re-do this step in that case.

(b) Automatically Correcting Bad Pixels

There are two varieties of bad pixels that can be automatically found and flagged by CUBISM: global level and record level bad pixels. For either case, your cube must first have been built before you can use either the automated Global or Record level bad pixel routines within CUBISM.

i. Global Level Automatic Bad Pixel Correction
In the CUBISM Project window, under the BadPix menu item in the top row, scroll down to the "Auto-gen Global Bad Pixels..." item and click on it. A small "AutoBadPix" pop-up window, displaying the first line "Automatic Global Bad Pixels," appears with default values of Sigma-Trim 5.00 and MinBad-Frac 0.10. Use these. There are two checkboxes toward the bottom of this window: "BG " and "UNC." Checking BG (clicking on its box turning it to dark instead of light gray) means that the Sigma-Trim is applied to the background subtracted data. We checked it. If UNC is set (i.e., the little box next to "UNC" is darkened), then the pipeline generated uncertainties are used. If not, a median absolute deviation is used as an estimate of the sigma value. We did not set it. Click "OK." In the CUBISM Project window, you will see a message: "Generating global auto bad pixels... done in 119.60 s with 86 badpix" (in our case).

ii. Record Level Automatic Bad Pixel Correction
In the CUBISM Project window, under the BadPix menu item in the top row, go down to "Auto-gen Record Bad Pixels..." Again, the small "AutoBadPix" pop-up window appears, this time displaying the first line "Automatic Record Bad Pixels." The default values this time are Sigma-Trim 5.00 and MinBad-Frac 0.75. Use these. We checked BG, unchecked UNC. Hit OK to run the algorithm. In the CUBISM Project window, you will see a message: "Generating record auto bad pixels... done in 42.45 s with 41294 badpix" for our case.

(c) Saving a Bad Pixel (.bpl) File

This is a good time to save a record of the bad pixels found so far by creating your "Bad Pixel" file for the first time. This is done under the BadPix menu item in the CUBISM Project window. Scroll down to and click on "Save Bad Pixels..." (the third menu item under "BadPix"). A pop-up window, "Save Bad Pixels As...," prompts you for the filename and directory path for your desired bad pixel file. For our example, we called it "irs_sl2.bpl."

Now, rebuild the cube.

(d) Saving Your Cube Project for the First Time

This is a good time to save your Cube Project. In the CUBISM Project window, select the first menu item, "File," and choose "Save As." You are prompted with a "Save Cube Project As..." pop-up window. In our case, we called this Cube Project "irs_sl2.cpj." In the CUBISM Project window, a message appears "Saving project to irs_sl2.cpj (no data, no accts) done 41.9 MB." At this juncture, should you decide to quit the program, the next time you invoke CUBISM, you can just read in this CUBISM project file and re-build the Cube, without having to specify the data or background records, or the aperture that excludes the ratty pixels on the slit edges. Remember, you will also need to specifically re-load any Bad Pixel File you may have saved using the BadPix → "Load and Append Bad Pixels..." menu item, and then "QuickBuild" your cube in order to flag any additional bad pixels you might

have designated using either the "Auto-Gen Global" or "Auto-Gen Record" level BadPix menu items or the Pixel Backtracking Tool.

(e) Checking Results of Automatic Bad Pixel Removal
Now, examine the result from part 4. (b) above. From the CUBISM Project window, select the fourth menu item along the top, the "Cube" button. Choose View Cube (new viewer) that way your old CubeView window (assuming it was up) does not get erased off the screen when the channel map display comes up. You can now step through your channel (wavelength) maps individually, comparing their appearance before and after the automatically generated bad pixel removal steps.

In our case, the default values for the automatic bad pixel finding worked really well in that when we stepped through the individual channel maps with bad pixels removed (in the automated process) and without any bad pixels removed, no real (faint) features disappeared due to the automated process bad pixel removal scheme. For us, this was *almost* enough for bad pixel removal. Artifacts that remained were at the level of the noise, or not much above. Only in cases where such artifacts could interfere with a 1-D extracted spectrum, or with the production of a 2-D channel map, did we go back and perform bad pixel removal "by hand" (see the next section).

(f) Correcting Bad Pixels (Global or Record Level) by Hand

i. Manual (Bad) Pixel Backtracking: Identifying and Correcting Bad Pixels
Use of this tool assumes that your Cube Project is loaded into CUBISM and that you have a CubeView display of your data in which you can step through your individual (spectral) channel maps. For our SL2 data, we have 77 spectral channels. The CubeView window allows you to view your spectral channels in "movie" mode, autoscaling each spectral channel map individually to a sensible set of gray levels, depending on the minimum and maximum data values in each spectral map. (If you do not like the default grayscale levels, you can use the "Scale Image with Histogram Tool" (second icon from the left in the top line's Icon Menu), which will scale each channel to the levels found within a box whose size and location you specify). Stepping through your channels in this way, any vertical striping artifact in your maps will become obvious. Such vertical striping is caused by the intermittent (in time) "hot" pixel, or a small group of "hot" pixels during mapping. It is up to you to decide whether or not any artifact like this is worth removing from/correcting for in your data. If such "hot" pixels would adversely affect any integrated line map (see Section 5 below) you would like to produce, or would introduce spurious "features" into an extracted spectrum (see Section 6 below), then it is worth your time to correct such errant pixels. Otherwise, it is not worth your time.

Now, suppose you have a channel with the offending stripes displayed in the CubeView window. You now click on the icon of the "Pixel BackTracking Tool," which is the 8th icon from left along the top row of icons. Left-click on an offending (hot) pixel. This will mark that pixel with a green "x" and freeze the tool, so you can navigate over to the "BackTracking: IRS_SL2 (in our case)" window that appears. This window displays all of the pixels from all of the records that contributed to the particular pixel you just marked with a green "x" in the CubeView window. Scrolling down the list of records displayed in the "BackTracking" window, look for anomalous values in the "(Val−Back)" (Value−Background) column, and identify which pixel is producing these.

If you find the same persistent bad pixel causing anomalous values in all (or most) of the displayed records, then choose (highlight) just one of the lines that lists the bad pixel in any of the displayed records. Once a pixel within a record is highlighted in this way within the "BackTracking" window, your mouse is enabled to "right-click" (hold down the Apple key and click for a Mac laptop), which action will bring up a "context menu." You are given three options: "Bad Pixel (Global)," "Bad Pixel (This Record)," or "Bad Pixel (These Records)." These are your options for how to flag the pixels that are contributing to the one you have marked with a green "x" in the CubeView window. For example, suppose you choose (click on) "Bad Pixel (These Records)" within this "context menu." This action will darken the indicator circle to the left of this choice, informing you that your choice has now been recorded. However, in order to effect your choice, you must return to the CUBISM Project window and click on the "QuickBuild" radio button at the bottom of the screen. NB: the "QuickBuild" option appears as a menu item within the CUBISM Project window when you are in Pixel BackTracking mode. Once the cube is (quickly) rebuilt, your channel map will be re-displayed with the offending pixel corrected for in the display. Repeat this procedure to correct other hot pixels in your displayed channel map. However, in order to get rid of an entire stripe of hot pixels, if the artifact you were trying to get rid of still appears in your channel map, but the single pixel you had marked with the green "x" with the Pixel BackTracking tool is now corrected, you can choose a hot pixel immediately below the one you just corrected, click on it, and repeat the above steps, except this time, when the "context menu" comes up, try "Bad Pixel (Global)," instead. This action will remove said pixel from all of your data. Remember to "QuickBuild" again in the CUBISM Project window to see the effect of this action. Often, this will remove the offending stripe. If so, you must save the results of your work into a bad pixel (.bpl) file.

ii. Manual (Bad) Pixel Backtracking: Undoing Bad Pixel Correction
Suppose you have indicated a pixel to be bad, rebuilt your cube using "QuickBuild," re-displayed the result, and find that marking this pixel had essentially no effect on the quality of your channel

map. In that case, there is no point in leaving this pixel flagged. To unflag it, simply repeat the exact same steps you carried out to flag the pixel in the first place, only now when the "context menu" appears when you right-click the highlighted pixel in the "BackTracking" window, click the same option you chose previously to toggle the option to de-select it (the circle next to your choice is now light gray, instead of black), re-build your cube using "QuickBuild," and you are done.

iii. Saving Bad Pixels Identified with the Pixel Back-Tracking Tool

Once you have identified some (enough) bad pixels with the Pixel BackTracking Tool, and have re-built your cube each time with QuickBuild, you can save your work into your Bad Pixel File, (.bpl), by going over to the CUBISM Project Window, pulling down on the BadPix menu item from the top line, and choosing "Save Bad Pixels." A pop-up window, entitled: "Save Bad Pixels As..." comes up. You can either create a new .bpl file (if you do not already have one) to save your work to, or simply click on the current Bad Pixel file you are using ("irs_sl2.bpl" in our case). Click OK once you have specified your .bpl file. In our case, since we have specified a file that already exists, a pop-up window entitled: "Overwrite?" comes up with the disturbing message: "Overwrite irs_sl2.bpl?" Your only options are Yes and No. Click Yes. All that happens is that the existing bad pixel file (assuming you have one) is merely appended to.

iv. Re-Loading Your Bad Pixel File Next Time You Start up Your Work

We have already noted that once you have saved your CUBISM project to a .cpj file, "irs_sl2.cpj" in our case, and your Background Records to a background (.bgl) file, "irs_sl2.bgl" in our case, you can re-load said CUBISM project next time you fire up CUBISM. You must re-build your cube, however. Once your cube is re-built, you can verify, using the Info pull-down menu that the backgrounds have properly been accounted for. Make sure you also open a CubeView window at this juncture, by clicking on the View Cube radio button. To your dismay, you will note that all those stripes you worked so hard to get rid of, are still there! In order to recover your work, for all the bad pixels you determined using the BackTracking Tool and had saved to a .bpl (Bad Pixel file), "irs_sl2.bpl" in our case, there are *two* more steps: (i) in the CUBISM Project window, under the BadPix menu item, you must pull down to and click on "Load and Append Bad Pixels...," which will open up a window prompting you to choose which Bad Pixel file to load, and (ii) to effect that bad pixel file, after you have loaded it in, you have to click on the "QuickBuild" radio button (which is now enabled, since you read in your Bad Pixel file that has BackTracked bad pixels specified in it). You can watch the artifacts in your CubeView channel map display window disappear again.

(g) Viewing Your Uncorrected and Bad Pixel Corrected Data Cubes Simultaneously

Suppose you have re-loaded your CUBISM project, "irs_sl2.cpj" in our case, and have gone through the steps outlined in 4. (f) iv. above to read in and apply (via QuickBuild) your previously saved Bad Pixel file, in our case, "irs_sl2.bpl." You have clicked on the CubeView radio button to view the individual channel maps in your bad-pixel corrected cube. Now, suppose you would like to, at the same time, view your data cube without the bad-pixel corrections having been applied, for a direct channel by channel comparison. Doing so will require you to go back to your CUBISM Project Window, use the File pull-down menu item at the top, and choosing the "Open..." option. The "Load Cube Project" window will appear, you can specify your same cube project file, "irs_sl2.cpj" in our example, which will open a new Cube Project window. You will need to re-build your cube again, but this time you will not load and append your Bad Pixel file. Instead, just click on the CubeView radio button from this new instance of the Cube Project window, and lo and behold, a second CubeView window will appear, displaying the uncorrected data.

5. Creating an Integrated Channel Map

Suppose you would like to create a flux-calibrated, continuum-subtracted, integrated emission-line map of several spectral lines of one molecule—in our case the sum of the H_2 emission lines that appear in the SL1 module: 8.0 μm, 9.7 μm, and 12.3 μm.

(a) Creating a Spectrum

You must first create a 1-D spectrum before you can create a 2-D channel map! Suppose you have your Cube Project loaded and re-built (as outlined in 4. (f) above), and have a CubeView window open (by having clicked on the "View Cube" radio button at the bottom of the CUBISM Project window). You must next open a CubeSpec window. A good way to do this is to first display a channel that has some line emission of interest in it, just to orient yourself. Next, click on the "Extract Spectra and Stack Cubes" icon (7th from the left at the top of the CubeView window). Hit the "x" key (for extract) and drag the mouse from the top left to the bottom right of a rectangular region for which you'd like to extract the spectrum (this is the reason it is a good idea to display a channel with line emission in it first). Immediately, a CubeSpec window pops up, with its title displaying the pixel coordinates of your rectangular region. You can drag the rectangular aperture around by dragging on one of its magenta edges, or using your keyboard arrow keys, and you can resize your extraction aperture by dragging on the bottom right corner "handle." The spectrum displayed in the CubeSpec window changes with the aperture.

(b) Specifying the Line(s) to Integrate Over

You must choose the "Map" (vs. "Full Cube") option at the top of the CubeSpec window to allow you to define your desired line channels and continuum level(s). To define your line regions in the displayed spectrum, choose the "Peak" option hidden under the "Continuum" button. When this button displays

"Peak," use your mouse to define the lower and upper wavelength limits defining each line you would like to integrate over. To do this, place the vertical bar (by dragging it with the mouse) to the left of your spectral line of choice, click, then place the vertical bar to the right of your spectral line (by dragging it with the mouse), and click to record the upper wavelength limit of your line. Repeat for as many lines as you would like to integrate over. Each line region you have specified will be shaded in orange.

Once you are satisfied with your chosen lines, set the value of the "Peak" radio button back to "Continuum." You are now free to specify as many continuum regions in the spectrum as you like, in the same fashion you did for the lines. Your chosen continuum regions will be highlighted in maroon. Once your continua are specified, click the "Integrate" button. This will convert the map displayed in your CubeView window to continuum-subtracted, pure integrated line emission in W m^{-2} sr^{-1} units. CAUTION: If you *do not* hit the integrate button, the resulting map will not be continuum-subtracted, and will remain in MJy sr^{-1} units!

(c) Saving/Exporting Your Integrated Line Intensity Map

Play with the grayscale until it displays as you like it. In the CubeView window, click on the Options menu item, and pull-down to "Set Scale Range." A pop-up window, "Scaling" comes up, allowing you to enter the low and high data values between which to scale your image. You can specify the type of scaling (linear, logarithmic, etc.) using the "Scale Image" option under the same Options menu item in the CubeView window.

Once you are satisfied with your display, in order to save your integrated line intensity map, in the CubeView window, under the File menu, pull-down to "Save Map as FITS." A "Save Map as File" pop-up window appears in which you can specify the filename and the directory in which you would like CUBISM to save your map. The default directory for CUBISM to write files out to is the one you specified when you created your CUBISM Project. In our case, this was "/Users/fun/Documents/Projects/IRS_ScanMap/BCD_17Aug07/."

(d) Saving a Simulated 8 μm (Band 4) IRAC Map

Follow the steps outlined in 5. (a) above. Choose the "Map" (vs. "Full Cube") option at the top of the CubeSpec window. Under the Maps menu item at the very top of the CubeSpec window, pull-down to IRAC 8.0 μm. Immediately, the 8.0 μm filter bandpass of the IRAC camera is outlined in orange on top of your displayed spectrum. At the same time, the simulated (from your IRS data) 8.0 μm integrated flux map appears in the CubeView window, in MJy sr^{-1} units. Follow the steps for saving the simulated 8.0 μm map outlined in 5. (c) above.

6. Extracting a 1-D Spectrum

Just a cautionary note: CUBISM will produce output spectra for only one IRS module at a time. So, should you want to "stitch" the SL1 and SL2 spectra into a single spectrum, for display, publication, or further measurement, fitting, or processing, you would need to write your own IDL (or SM) code to read in the ASCII .tbl files CUBISM generates to further manipulate the spectra. This includes plotting of the resultant combined spectrum.

(a) Extracting a 1-D Spectrum over a User-Specified Aperture

Follow the steps in 5. (a) above to create a 1-D spectrum in a CubeSpec window. Set the position and size of your aperture to your liking in the CubeView window. On the File menu item in the CubeSpec window, choose "Save Spectrum As." This will open a pop-up window which will prompt you for the filename and directory in which to place the 1-D spectrum. You have a choice of output formats: an ASCII table format output (extension .tbl) or a FITS-file output (output extension .fits).

(b) Line Flux Measurement

CUBISM also has the capability of allowing you to measure the line flux in a given aperture. Assuming you already have your spectrum (sampled over your desired aperture) displayed as outlined in 6. (a) above, click on the "Map" (as opposed to "Full Cube") option in the CubeSpec window. This allows you to specify the wavelength regions for your desired line and continuum level(s). Follow the instructions in 5. (b) above to specify your desired line and continuum level(s), and then click on the "Fit" button in the CubeSpec window. The line-fit parameters (average continuum level, equivalent width (in μm), the peak line intensity (in MJy sr^{-1}), the peak line wavelength, the median line intensity, median line wavelength, and the wave-length integrated line strength, in mixed units of MJy sr^{-1} $\times$ μm, will be displayed in the upper right corner of the CubeSpec window. At the same time, the fit to the continuum in the wavelength region you specified, will be plotted; a star symbol is plotted at the location of the fitted line peak, and a hashed region will indicate the line's equivalent width.

(c) ds9 Regions

CUBISM allows you to read in *only two varieties of ds9 regions: circles and polygons*. Suppose you have loaded a .FITS image into ds9 on which you wish to specify regions in which you would like to determine the integrated line strength of a line or spectral feature in your IRS data. You can only specify these ds9 regions as circles or polygons. WARNING: ds9 makes a distinction between "Box" and "Polygon" regions. Under the "Region" menu in ds9, click on the "Shape" option. A whole menu of possibilities comes up, including circle, ellipse, box, polygon, line, etc. Note that if you have "Box" inadvertently checked, instead of "Polygon" for specifying a cubical or rectangular region, the resulting ds9 output region file cannot be read into CUBISM! You must have polygon checked instead.

Assuming you have the proper format region file produced by ds9, you can read this into CUBISM. Assuming you have your CubeView window open, use the File pull-down menu item. Select "Extract Region from File" and the "Read Region from File" pop-up window will appear, allowing you to specify the directory path and filename of the ds9 region you would like CUBISM to read in. Click OK, and the region you specified will be displayed in your CubeView

window, and the spectrum integrated over that region will be displayed in the CubeSpec window. CAVEAT: although you can specify many regions in a single output ds9 regions file, CUBISM can only read in a ds9 region file that specifies one single contiguous region. If you would like to measure line parameters in several different regions specified using ds9, you must write out as many ds9 region files as you have regions of interest, in order to read these into CUBISM individually.

REFERENCES

Abergel, A., et al. 1996, A&A, 315, 329
Amiaud, L., Momeni, A., Dulieu, F., Fillion, J. H., Matar, E., & Lemaire, J.-L. 2008, Phys. Rev. Lett., 100, 056101
André, P., Ward-Thompson, D., & Barsony, M. 1993, ApJ, 406, 122
Arce, H. G., & Sargent, A. I. 2005, ApJ, 624, 232
Bacmann, A., André, P., Puget, J.-L., Abergel, A., Bontemps, S., & Ward-Thompson, D. 2000, A&A, 361, 555
Barsony, M., et al. 2005, BAAS, 37, 1251
Bertoldi, F., Timmermann, R., Rosenthal, D., Drapatz, S., & Wright, C. M. 1999, A&A, 346, 267
Bontemps, S., et al. 2001, A&A, 372, 173
Brooke, T. Y., Tokunaga, A. T., & Strom, S. E. 1993, AJ, 106, 656
Buch, V., & Devlin, J. P. 1994, ApJ, 431, L135
Cabrit, S., Flower, D. R., Pineau des Forêts, G., Le Bourlot, J., & Ceccarelli, C. 2004, Ap&SS, 292, 501
Chernin, L. M., & Masson, C. R. 1991, ApJ, 382, 93
Chernin, L. M., Masson, C., Gouveia dal Pino, E. M., & Benz, W. 1994, ApJ, 426, 204
Codella, C., Cabrit, S., Gueth, F., Cesaroni, R., Bacciotti, F., Lefloch, B., & McCaughrean, M. J. 2007, A&A, 462, L53
Colgan, S. W. J., Schultz, A. S. B., Kaufman, M. J., Erickson, E. F., & Hollenbach, D. J. 2007, ApJ, 671, 536
Cunningham, A. J., Adam, F., Varnière, P., Mitran, S., & Jones, T. W. 2009, ApJS, 182, 519
Cunningham, A. J., Thorndike, S. L., Frank, A., Quillen, A. C., & Blackman, E. G. 2005, PPV, LPI Contrib. No., 1286, 8426
Cyganowski, C. J., et al. 2008, AJ, 136, 2391
Dabrowski, I. 1984, Can. J. Phys., 62, 1639
Dartois, E. 2005, Space Sci, Rev., 119, 293
DeVito, B., & Hayward, T. L. 1998, ApJ, 504, L43
Dionatos, O., Nisini, B., Garcia Lopez, R., Giannini, T., Davis, C. J., Smith, M. D., Ray, T. P., & De Luca, M. 2009, ApJ, 692, 1
Draine, B. T., & Anderson, N. 1985, ApJ, 292, 494
Draine, B. T., & Lee, H. M. 1984, ApJ, 285, 89
Fazio, G., et al. 2004, ApJS, 154, 10
Flaherty, K. M., Pipher, J. L., Megeath, S. T., Winston, E. M., Gutermuth, R. A., Muzerolle, J., Allen, L. E., & Fazio, G. G. 2007, ApJ, 663, 1069
Flower, D. R., & Watt, G. D. 1984, MNRAS, 209, 25
Flower, D. R., & Watt, G. D. 1985, MNRAS, 213, 991
Gâlfalk, M., & Olofsson, G. 2007, A&A, 475, 281
Hanner, M. S., Brooke, T. Y., & Tokunaga, A. T. 1995, ApJ, 438, 250
Houck, J. R., et al. 2004, Proc. SPIE, 5487, 62
IRAC Data Handbook 2006, (http://ssc.spitzer.caltech.edu/irac/dh)
Khanzadyan, T., Gredel, R., Smith, M. D., & Stanke, T. 2004, A&A, 426, 171
Kristensen, L. E., Ravkilde, T. L., Field, D., Lemaire, J. L., & Pineau des Forêts, G. 2007, A&A, 469, 561
Le Bourlot, J., Pineau des Forêts, G., & Flower, D. R. 1999, MNRAS, 305, 802
Lee, C.-F., Ho, P. T. P., Palau, A., Hirano, N., Bourke, T. L., Shang, H., & Zhang, Q. 2007, ApJ, 670, 1188
Loinard, L., Torres, R. M., Mioduszewski, A. J., & Rodríguez, L. F. 2008, ApJ, 675, L29
Looney, L. W., Tobin, J. J., & Kwon, W. 2007, ApJ, 670, L131
Maret, S., et al. 2009, ApJ, 698, 1244
Matthews, L. D., Greenhill, L. J., Goddi, C., Chandler, C. J., Humphreys, E. M., & Kunz, W. 2010, ApJ, 708, 80
Motte, F., André, P., & Neri, R. 1998, A&A, 336, 150
Neufeld, D. A., et al. 2006, ApJ, 649, 816
Neufeld, D. A., et al. 2009, ApJ, 706, 170
Noriega-Crespo, A., et al., ApJS, 154, 352
Oliveira, J., et al. 2010, ApJ, 714, 778
Padgett, D., Brandner, W., Stapelfeldt, K., Strom, S. E., Terebey, S., & Koerner, D. 1999, AJ, 117, 1490
Park, T. J., & Light, J. C. 1989, J. Chem. Phys., 91, 974
Rathborne, J. M., Jackson, J. M., Chambers, E. T., Stojimirovic, I., Simon, R., Shipman, R., & Frieswijk, W. 2010, ApJ, 715, 310
Ressler, M. E., & Barsony, M. 2001, ApJ, 584, 832
Rieke, G. H. 2007, ARA&A, 45, 77
Rosen, A., & Smith, M. D. 2003, MNRAS, 343, 181
Rosen, A., & Smith, M. D. 2004, MNRAS, 347, 1097
Rosenthal, D., Bertoldi, F., & Drapatz, S. 2000, A&A, 356, 705
Schofield, K. 1967, Planet. Space Sci., 15, 643
Shroyer, B., Cunningham, A. J., Frank, A., Poludnenko, A., Jones, T., Yirak, K., & Carroll, J. 2009, BAAS, 41, 695
Siebenmorgen, R., & Krügel, E. 1992, A&A, 259, 614
Siegbahn, P., & Liu, B. 1978, J. Chem. Phys., 68, 2457
Smith, J. D., et al. 2007, PASP, 119, 1133
Smith, M. D., & Rosen, A. 2005a, MNRAS, 357, 1370
Smith, M. D., & Rosen, A. 2005b, MNRAS, 357, 579
Stanke, T., Smith, M. D., Gredel, R., & Khanzadyan, T. 2006, A&A, 447, 609
Steinacker, J., Bacmann, A., Henning, Th., Klessen, R., & Stickel, M. 2005, A&A, 434, 167
Tamura, M., Gatley, I., Waller, W., & Werner, M. W. 1991, ApJ, 374, L25
Tobin, J. J., Hartmann, L. W., Calvet, N., & d'Alessio, P. 2008, ApJ, 679, 1364
Tobin, J. J., Hartmann, L. W., Looney, L. W., & Chiang, H. S. 2010, ApJ, 712, 1010
Tobin, J. J., Looney, L. W., Mundy, L. G., Kwon, W., & Hamidouche, M. 2007, ApJ, 659, 1404
Tokunaga, A. T., Sellgren, K., Smith, R. G., Nagata, T., Sakata, A., & Nakada, Y. 1991, ApJ, 380, 452
Velusamy, T., & Langer, W. D. 1998, Nature, 392, 685
Werner, M. W., et al. 2004, ApJS, 154, 1
Whitney, B. A., Wood, K., Bjorkman, J. E., & Cohen, M. 2003, ApJ, 598, 1079
Wilgenbus, D., Cabrit, S., Pineau des Forêts, G., & Flower, D. R. 2000, A&A, 356, 1010
Wolniewicz, L., Simbotin, I., & Dalgarno, A. 1998, ApJS, 115, 293
Ybarra, J. E., Barsony, M., Haisch, K. E., Jr., Jarrett, T. H., Sahai, R., & Weinberger, A. J. 2006, ApJ, 647, L159
Zhang, M., & Wang, H. 2009, AJ, 138, 1830